CFD simulations of a pitching aerofoil for the study of dynamic stall

Author
Francisco Javier Forriol Fernández

Master thesis submitted under the supervision of
Prof. Dr. Mark Runacres

the co-supervision of
PhD. Stud. Luca Damiola

in order to be awarded the Master's Degree in
Electromechanical Engineering

Academic year
2021-2022

ULB UNIVERSITÉ LIBRE DE BRUXELLES

ULB UNIVERSITÉ LIBRE DE BRUXELLES

Exemplaire à apposer sur le mémoire ou travail de fin d'études,
au verso de la première page de couverture.

Réservé au secrétariat :	**Mémoire réussi***	**OUI**
	NON	

CONSULTATION DU MEMOIRE/TRAVAIL DE FIN D'ETUDES

Je soussigné

NOM :
Forriol Fernández ……………………………………………………………………………
………………………

PRENOM :
Francisco Javier ……………………………………………………………………………
………………..

TITRE du travail :
CFD simulations of a pitching aerofoil for the study of dynamic ……………………………
stall ………

……………………………………………………………………………………………
…………………………………

[✓ **AUTORISE***]

~~**REFUSE***~~

la consultation du présent mémoire/travail de fin d'études par les utilisateurs des bibliothèques de l'Université libre de Bruxelles.

Si la consultation est autorisée, le soussigné concède par la présente à l'Université libre de Bruxelles, pour toute la durée légale de protection de l'œuvre, une licence gratuite et non exclusive de reproduction et de communication au public de son œuvre précisée ci-dessus, sur supports graphiques ou électroniques, afin d'en permettre la consultation par les utilisateurs des bibliothèques de l'ULB et d'autres institutions dans les limites du prêt inter-bibliothèques.

Formulaire version 04/2015

** Biffer la mention inutile*

Fait en deux exemplaires, **Bruxelles, le** 02/06/2022 **…………..**

Signature

** Biffer la mention inutile*

If I have seen further it is by standing on the shoulders of giants.

Isaac Newton

Abstract

CFD simulations of a pitching aerofoil for the study of dynamic stall, by Francisco Javier FORRIOL FERNÁNDEZ. Master's degree in Electromechanical Engineering - Aeronautics specialization. Academic year: 2021-2022.

Dynamic stall (DS) is a non-linear unsteady phenomenon that occurs in an airfoil when a rapid incidence increase is produced. It has a crucial relevance in industrial applications such as helicopter rotor aerodynamics or wind turbines. In this project, a study of DS for the NACA0018 aerofoil is carried out using OpenFOAM. Detached Eddy Simulations (DES), 2D Unsteady Reynolds Averaged Navier-Stokes (URANS), and 3D URANS approaches are tested, including several turbulence models: Spalart-Allmaras, k-ω SST and Langtry-Menter k-ω SST. Computational Fluid Dynamics (CFD) simulations performed include static, dynamic quasi-steady sweeps and dynamic stall cases. Results are validated using wind tunnel measurements from Strangfeld et al. It is found that 2D URANS k-ω SST simulations represent an excellent trade-off between accuracy and computational cost, correctly predicting the main physical events of the DS phenomenon. Besides, the results of the parametric studies demonstrate that the increase of the motion frequency and amplitude produces an increase in the maximum lift coefficient, a delayed dynamic stall onset, an enlargement of the stall strength, and a growth of the hysteresis loop size.

Key words: Dynamic Stall (DS), pitching aerofoil, NACA0018, OpenFOAM, Computational Fluid Dynamics (CFD), Unsteady Reynolds Averaged Navier-Stokes (URANS).

Acknowledgements

To my **giants**:

I would like to start expressing my gratitude to the people who have helped me while developing my thesis: my supervisor, Professor Mark Runacres, for trusting me and for your advice during the process; and my co-supervisor, Luca Damiola, for your availability, dedication and teachings throughout these months.

I would like to warmly thank the FSUPV Team family for the life-changing experience I had at the team last year. It was an unbeatable season of pure dedication, growing, passion, and fulfilment. Especial acknowledges to Víctor, Joan and Juanjo for your patience, advice and support. I can't wait to see what the future will bring to you.

Lastly, I would like to thank all the people that have been by my side during these years. Thanks to *cafeteros* for sharing every step of this long journey with me. Thanks to my sister, Bea, for making life seem a little easier with her support and comprehension. Thanks to my niece María for making it seem more lovely. Thanks to my parents for their tireless effort to allow me to achieve all my goals and make me happy; I would never have arrived here without you.

Contents

1 Introduction **1**
- 1.1 Objectives 3
- 1.2 Content 4
- 1.3 State of the art 4
- 1.4 Dynamic Stall 6
- 1.5 Turbulence modelling 10

2 Methods **12**
- 2.1 Case description 12
- 2.2 Conceptual modelling 14
- 2.3 Geometry, domain and boundary conditions 14
- 2.4 Meshing 16
- 2.5 Solver setup 23
- 2.6 Turbulence modelling 24
- 2.7 Convergence criteria 27

3 Results and discussion **28**
- 3.1 Quasi-steady motion 28
- 3.2 Fast sweeps 42
- 3.3 Dynamic stall analysis 43
- 3.4 Dynamic stall influences 50

4 Conclusions and future developments **55**

Bibliography 57

List of Figures

1.1 Creation of new CFD turbulence models and evolution of the number of wind tunnel tests in the last decade at Boeing [1]. 1
1.2 On the left, Particle Image Velocimetry (PIV) measurements of dynamic stall [2]. On the right, CFD Large Eddy Simulation (LES) of dynamic stall [3]. 2
1.3 On the left, helicopter DS during forward motion [4]. On the right, scheme of a VAWT operation [5]. 3
1.4 Schematic representation of the different events of the dynamic stall process: (a) Attached flow, (b) Flow reversal, (c) Shear layer roll-up, (d) Stall onset, (e) Full stall, (f) Flow reattachment [2]. 7
1.5 Transition between the shear roll-up and the stall onset phases. In blue, clockwise vortices. In red, anticlockwise ones. Adapted from [6]. 8
1.6 On the left, light stall. On the right, deep stall scheme [7]. 8
1.7 On the left, comparison between lift coefficient in static and dynamic stall [7]. On the right, comparison between lift coefficient in light and deep dynamic stall [2]. 9
1.8 Dynamic stall development depending on the aerofoil relative thickness [8]. 10
1.9 At left, scheme of the different turbulence modelling approaches [9]. At right, example of solution using DNS, LES and RANS [10]. 11

2.1 Influence of reduced frequency and amplitude in the aerofoil's motion. 13
2.2 On the left, a conceptual scheme of the considered domain. On the right, the O-shape domain with a close-up of the NACA0018 at the centre. 15
2.3 Final mesh generated with *Pointwise* with close-ups to the leading edge, trailing edge and the boundary layer (wall $y^+ < 1$). 17
2.4 Wall y^+ through the aerofoil's surface for different angles of attack α in static cases. 17
2.5 Above, Mesh 1 with $GR = 1.1$ and $N = 26196$. Below, Mesh 3 with $GR = 1.06$ and $N = 103878$. 19
2.6 At the left, relative and extrapolated error of the fine and medium meshes. At the right, example of application of the Richardson's Extrapolation for $\alpha = 12$ deg. 20
2.7 In blue, extrapolated error for the coarse ($h = 0.25$ m), medium ($h = 0.20$ m) and fine ($h = 0.15$ m) meshes. In orange, dimensionless computational time respect to the medium mesh time. 21
2.8 Above, Mesh A with $GR = 1.06$ and 500 Aerofoil Points. Below, Mesh B with $GR = 1.1$ and 300 Aerofoil Points. 21

2.9 At the left, relative error of the tested meshes respect to the Mesh 2. At the right, extrapolated relative error of the four meshes. 22
2.10 At the left, residuals evolution during the iteration process. At the right, force coefficients variation evolution. 27

3.1 Experimental data by Strangfeld et al.[11] and Timmer et al.[12] for the quasi-steady upstroke (solid line) and downstroke (dashed line) motions.... 29
3.2 Evolution of the c_l with the angle of attack α for static cases (circles) compared with the experimental quasi-steady upstroke (solid line) and downstroke (dashed line) results of Strangfeld et al.[11]. 30
3.3 At the top, dimensionless velocity U/U_∞ field showing the Laminar Separation Bubble (LSB) evolution at $\alpha = 4$ deg and $\alpha = 8$ deg. At the bottom, pressure coefficient c_p comparison between k-ω SST and Langtry-Menter k-ω SST at $\alpha = 8$ deg. 31
3.4 At the top, dimensionless velocity U/U_∞ comparison between the RANS and the centre-line of the DES k-ω SST cases at $c_l = c_{lm}$. At the bottom, pressure coefficient c_p for the three k-ω SST cases at $c_l = c_{lm}$. 32
3.5 Comparison of dimensionless velocity U/U_∞ field between the RANS and DES k-ω SST cases at $\alpha = 24$ deg. 32
3.6 At the left, effect of turbulence intensity on the quasi-steady solution. On the right, influence of the motion's frequency in the quasi-steady solution. Upstroke in solid line, downstroke in dashed line. 34
3.7 At (a), evolution of the c_l with the angle of attack α during the quasi-steady upstroke (solid line) and downstroke (dashed line) motions for different turbulence models. At (b), close-up view of the maximum c_l zone. At (c), close-up view of the abrupt stall zone. 35
3.8 Comparison of the dimensionless velocity U/U_∞ between the k-ω SST and the SA cases before and after the abrupt stall angle, $\alpha = 19.2$ deg and $\alpha = 22.7$ deg, respectively. 36
3.9 At the top, comparison of the dimensionless z-axis vorticity $\omega_z c/U_\infty$ between the k-ω SST and the SA cases after the abrupt stall angle, $\alpha = 22.7$ deg. At the bottom, pressure coefficient c_p downstream of the leading edge (red dashed line) for both cases. 37
3.10 Influence of α_1 in the c_l vs α curve in the quasi-steady case. 38
3.11 Comparison between a 2D and 3D case during the quasi-steady upstroke (solid line) and downstroke (dashed line) motions. 39
3.12 Comparison of the dimensionless velocity U/U_∞ between the two-dimensional case and the three-dimensional (mid-span) one after the 3D abrupt stall, $\alpha = 20.66$ deg. 40
3.13 At the top, dimensionless velocity U/U_∞ before and after the abrupt stall for the three-dimensional case, $\alpha = 19.42$ deg and $\alpha = 20.26$ deg, respectively. At the bottom, the same but for the dimensionless vorticity field $\omega_z c/U_\infty$. 40
3.14 Comparison of the pressure coefficient c_p between Strangfeld et al. experimental data [11] and the URANS k-ω SST, Spalart-Allmaras and Langtry-Menter cases at $\alpha = 14.5$ deg with close-up to the suction peak and LSB zone. 41

3.15 Relative time cost for each tested approach for the quasi-steady motion in an unsteady simulation of 1 second. 42
3.16 Comparison of lift coefficient c_l results for fast sweep motions ($\alpha_0 = 2$ deg, $\alpha_1 = 2$ deg, $k = 0.08$ and $k = 0.263$) between experimental data by Strangfeld et al.[11], 2D and 3D cases. 43
3.17 At the top, lift coefficient c_l results of a deep dynamic stall case ($\alpha_0 = 14$ deg, $\alpha_1 = 14$ deg, $k = 0.063$) with key points indicated by letters. At the bottom, moment coefficient c_m for the same motion. Solid line for the upstroke, dashed line for the downstroke. 44
3.18 Pressure coefficient c_p plot, dimensionless velocity U/U_∞ and vorticity $\omega_z c/U_\infty$ for different incidences through the sweep motion ($\alpha_0 = 14$ deg, $\alpha_1 = 14$ deg, $k = 0.062$). 49
3.19 Comparison of the lift coefficient c_l results for a motion of $\alpha_0 = 14$ deg and $\alpha_1 = 10$ deg at different frequencies: $f = 0.4$ Hz, $f = 1$ Hz and $f = 1.6$ Hz. Upstroke in solid line and downstroke in dashed line. 50
3.20 Comparison of the dimensionless vorticity $\omega_z c/U_\infty$ around the aerofoil at the PDSV development instant for the small (1), medium (2) and high (3) frequency cases. 51
3.21 Comparison of the lift coefficient c_l results for a motion of $\alpha_0 = 14$ deg and $k = 0.063$ at different amplitudes: $\alpha_1 = 6$ deg, $\alpha_1 = 8$ deg, $\alpha_1 = 10$ deg and $\alpha_1 = 14$ deg. Upstroke in solid line and downstroke in dashed line. 52
3.22 Dimensionless velocity U/U_∞ field showing the light stall regime at $\alpha = 19$ deg (downstroke) for the low amplitude case ($\alpha_1 = 6$ deg). 53
3.23 Comparison of the lift coefficient c_l results for a motion of $\alpha_0 = 14$ deg and $k = 0.063$ at different amplitudes ($\alpha_1 = 6$ deg and $\alpha_1 = 14$ deg) using 2D and 3D simulations. Upstroke in solid line and downstroke in dashed line. ... 53
3.24 Comparison of the lift coefficient c_l results for a motion of $\alpha_0 = 14$ deg, $\alpha_1 = 14$ deg and $k = 0.063$ with different inlet turbulence intensities: $TI = 0.05\%$, $TI = 0.5\%$, $TI = 3.0\%$ and $TI = 7.5\%$. Upstroke in solid line and downstroke in dashed line. 54
3.25 Turbulence intensity evolution along with the x/R coordinate at $y/c = 0$ for the $TI = 7.5\%$ case. 54

List of Tables

2.1 Parametric studies considered in this project. 13
2.2 Fluid and flow properties used to simulate dynamic stall. 14
2.3 Pressure and Velocity boundary conditions in each patch for the 2D and 3D cases. 15
2.4 Parameters of the final structured mesh. 16
2.5 Parameters of the meshes considered for the Richardson's Extrapolation study. 19
2.6 Results for the coarse, medium and fine mesh at different angles of attack with the Richardson's Extrapolation parameters calculated. 20
2.7 Meshing parameters considered for the Aerofoil Points study. 22
2.8 Solver and smoother used for each equation at the steady case. 23
2.9 Solver and preconditioner used for each equation at the unsteady case. 23
2.10 Discretization schemes used for both the steady and unsteady cases. 24
2.11 Initial conditions used for the Spalart-Allmaras cases. 25
2.12 Initial conditions used for the k-ω SST cases. 26
2.13 Initial conditions used for the Langtry-Menter k-ω SST cases. 26

3.1 Motion parameters of the quasi-steady cases. 33

List of Abbreviations

2D	Two-Dimensional
3D	Three-Dimensional
BC	Boundary Condition
CFD	Computational Fluid Dynamics
DDES	Delayed Detached Eddy Simulation
DES	Detached Eddy Simulation
DS	Dynamic Stall
DSV	Dynamic Stall Vortex
EFD	Experimental Fluid Dynamics
HAWT	Horizontal Axis Wind Turbine
IDDES	Improved Delayed Detached Eddy Simulation
IV	Induced Vortex
LES	Large Eddy Simulation
LEV	Leading Edge Vortex
LSB	Laminar Separation Bubble
PDSV	Primary Dynamic Stall Vortex
PISO	Pressure-Implicit with Splitting of Operators
PIV	Particle Image Velocimetry
RANS	Reynolds Averaged Navier-Stokes
SA	Spalart-Allmaras
SDSV	Secondary Dynamic Stall Vortex
SIMPLE	Semi-Implicit Method for Pressure Linked Equations
SST	Shear Stress Transport
TEV	Trailing Edge Vortex
TI	Turbulence Intensity
TKE	Turbulence Kinetic Energy
URANS	Unsteady Reynolds Averaged Navier-Stokes
VAWT	Vertical Axis Wind Turbine

List of Symbols

α	Angle of attack	[deg]
α_0	Motion's mean angle	[deg]
α_1	Motion's amplitude	[deg]
α_{as}	Abrupt stall angle	[deg]
α_{ds}	Dynamic stall angle	[deg]
α_m	Maximum angle of attack	[deg]
α_{min}	Maximum angle of attack	[deg]
$\Delta c_{l_{as}}$	Lift coefficient drop	[-]
ϵ_{ij}	Absolute error	[-]
μ	Dynamic viscosity	[Pa·s]
μ_τ	Wall shear stress	[Pa]
μ_t	Kinematic turbulent viscosity	[m^2/s]
ν	Kinematic viscosity	[m^2/s]
$\bar{\nu}$	Modified turbulence viscosity	[m^2/s]
ω	Angular velocity	[rad/s]
ω_z	Z-component of vorticity	[s^{-1}]
ρ	Density	[kg/m^3]
c	Aerofoil's chord	[m]
C	Courant-Friedrichs-Levy Number	[-]
c_{l0}	Extrapolated lift coefficient	[-]
c_{lm}	Maximum lift coefficient	[-]
c_d	Drag coefficient	[-]
c_f	Friction coefficient	[-]
c_l	Lift coefficient	[-]
c_m	Moment coefficient	[-]
c_r	Richardson's Extrapolation fitting constant	[-]
e_{ij}	Relative error	[-]
e_{ij}^e	Extrapolated relative error	[-]
f	Frequency	[Hz]
GCI_{ij}	Grid convergence index	[-]
GR	Growth ratio	[-]
h	Representative cell length	[m]
k	Reduced frequency	[-]
M	Mach number	[-]
N	Total number of cells	[-]
N_y	Number of cells in y-direction	[-]
p	Order of convergence	[-]
r_{ij}	Cell length ratio	[-]
Re	Reynolds number	[-]

t	Time	[s]
TI	Turbulence intensity	[%]
U_∞	Free stream velocity	[m/s]
w	Aerofoil's span	[m]
y^+	Wall y^+	[-]
y_1	First cell size	[m]

Chapter 1

Introduction

Aerofoil aerodynamics has been a widely recurrent research topic since the beginning of the 20th century. The earliest theoretical and experimental studies focused on the static characteristics of aerofoils and, more concretely, on the low angle of attack and far from stall region due to its utility in the aviation industry.

Moreover, the importance of aerodynamics in multiple industry applications such as transportation or energy production has led to a growing interest in the Fluid Mechanics study, with notable improvements in the Experimental Fluid Dynamics (EFD) field.

The emergence of Computational Fluid Dynamics (CFD) during the last century and the recent improvement of computer calculation capabilities have also brought about a radical change. CFD allows studying a massive variety of fluid-related industrial problems reducing cost and time compared to classic EFD methods. Thus, the utilization of EFD techniques has suffered a significant usage reduction with the development of CFD tools such as reliable and affordable turbulence models (Figure 1.1). However, they are still necessary to correlate results and validate CFD calculations.

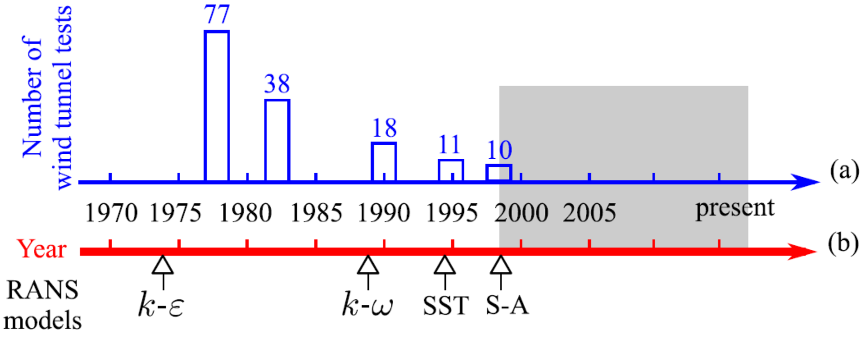

Fig. 1.1: Creation of new CFD turbulence models and evolution of the number of wind tunnel tests in the last decade at Boeing [1].

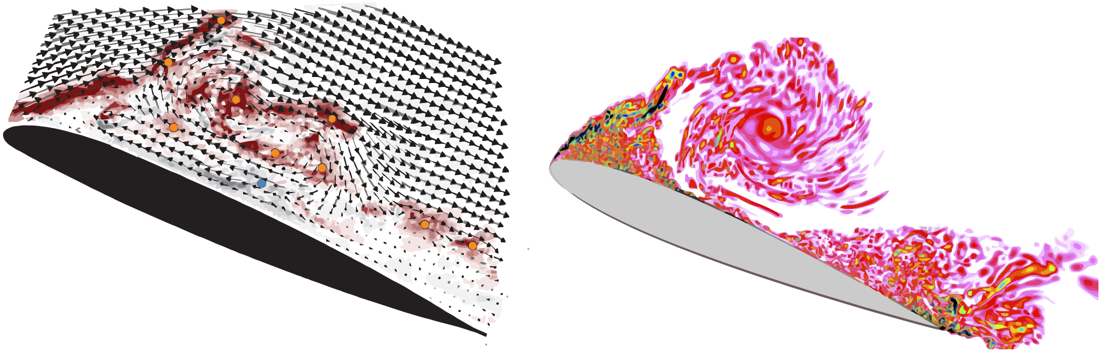

Fig. 1.2: On the left, Particle Image Velocimetry (PIV) measurements of dynamic stall [2]. On the right, CFD Large Eddy Simulation (LES) of dynamic stall [3].

In this way, the improvement in the research methodologies has implied the study of more complex aerodynamic phenomena, including unsteady and turbulent flows, such as dynamic stall (Figure 1.2).

Dynamic stall (DS) is a non-linear aerodynamic phenomenon that occurs in an aerofoil when a rapid increase in the angle of attack is produced. A delay in the stall angle characterizes it, as well as a lift overshoot and hysteresis, and a more severe and persistent stall than in the static case [13]. Furthermore, the most distinctive flow feature is the formation and breakdown of a large-scale turbulent structure called the dynamic stall vortex (DSV).

Historically, one of the most studied applications regarding dynamic stall has been helicopter rotor aerodynamics. During forward fly, relative airflow decreases in the retreating blades. It so does lift, which makes the blade flap downwards to compensate for lift asymmetry, enlarging its angle of attack and therefore causing dynamic stall (Figure 1.3).

Moreover, dynamic stall plays an essential role in wind turbine energy generation. On the one hand, it is required to properly determine the power output of conventional Horizontal Axis Wind Turbines (HAWT), where changes in local flow conditions can lead to dynamic stall. On the other hand, through Vertical Axis Wind Turbine (VAWT) operation, blades are rotating around the vertical axis, experiencing a considerable change in the incidence conditions (Figure 1.3), which may result in DS, being a relevant phenomenon for achieving a good aerodynamic efficiency [14].

Although dynamic stall has some beneficial features as the stall delay or lift increase, it is essential to remark that the large forces variation and the vortex breakdown can cause significant vibrations and structural loads. Thus, that must be kept in mind during the design phase, especially in the fatigue study.

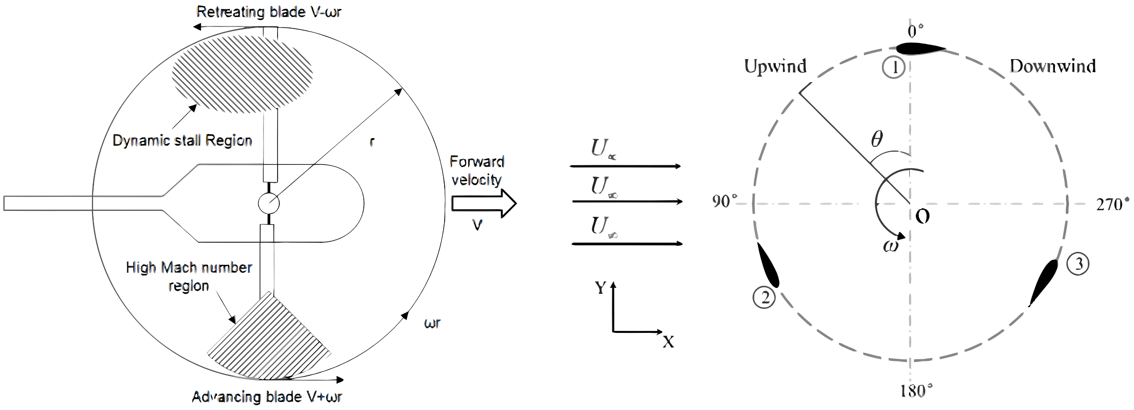

Fig. 1.3: On the left, helicopter DS during forward motion [4]. On the right, scheme of a VAWT operation [5].

Despite the apparent relevance of dynamic stall in the industry, the phenomenon is not fully understood. Its complexity also makes it difficult to model it. On this project, CFD simulations of a pitching NACA0018 aerofoil will be made to study dynamic stall. The analysis is focused on the interpretation of the physical phenomena and the development of an optimal CFD setup in terms of accuracy and computational affordability. For this, different modelling approaches are compared and discussed, including 2D, 3D and turbulence models. Moreover, a parametric study is done to determine the influence of motion's frequency, amplitude and inlet turbulence intensity in the DS.

1.1 Objectives

The project's main purpose is to study dynamic stall for the NACA0018 aerofoil using CFD simulations. Base on this, project objectives are defined:

- To develop a CFD setup using OpenFOAM that gives accurate results without a prohibitively expensive computational cost. For this, several sub-objectives are defined:
    - To analyse the accuracy of two and three-dimensional Unsteady Reynolds Averaged Navier-Stokes (URANS) simulations for modelling the dynamic stall phenomenon, both qualitatively and quantitatively.
    - To determine the best turbulence model for simulating dynamic stall using the URANS approach.
    - To assess the computational cost of three-dimensional Detached Eddy Simulations (DES) for the dynamic stall calculation. Besides, to determine the actual enhancement of the flow behaviour prediction compared with two-dimensional URANS simulations.

- To study the influence of motion's amplitude, reduced frequency and inlet turbulence intensity on dynamic stall for the NACA0018 using CFD simulations.

1.2 Content

The remainder of this chapter will be focused on analysing the state of the art and the dynamic stall principles. Also, the turbulence modelling approaches available when using CFD are briefly discussed. Chapter 2 explains the methodology of the thesis, which is mainly about the CFD process carried out using OpenFOAM, with particular attention to the mesh independence study using Richardson's Extrapolation. Then, Chapter 3 describes all the results obtained from the project, splitting the analysis into the different types of motion considered. Lastly, Chapter 4 shows the conclusions that have been deducted from the thesis elaboration and proposes future works to continue the analysis.

1.3 State of the art

Since the beginning of the seventies, several efforts have been focused on understanding, measuring and modelling dynamic stall from different perspectives. McCroskey et al. reports [15, 13] on dynamic stall tried to shed light on the phenomena understanding from a theoretical and physical point of view, splitting dynamic stall into different phases and determining the factors that most influence it.

From an experimental point of view, aerofoil load measurements in wind tunnels have been a recurrent topic, especially applied to the NACA0012 aerofoil [16, 17, 18]. Studies including NACA0018 aerofoil have also been performed, both on static [19, 20] and dynamic conditions. Wickens [21] and Raghunathan et al.[22] operated in high Reynolds number flows ($Re > 10^6$) while Strangfeld et al.[11] did it in lower ones ($Re = 3 \cdot 10^5$). Strangfeld et al. also warned about the importance of the interaction of the wind tunnel walls and the prototype and demonstrated the influence on the measurements, mostly on high stall conditions. Timmer et al.[12] explored a wide range of Reynolds numbers ($10^5 \leq Re \leq 10^6$).

In addition, remarkable experimental efforts using PIV have been made by Mulleners et al. to assess the onset of dynamic stall [7] and to give a more detailed description of the DS development [2]. On the other hand, Swalwell et al.[23] demonstrated the sensibility of far-field turbulence intensity (TI) on the wind tunnel measurements, where higher TI lead to a delayed stall.

Finally, it is important to remark on the work of Geissler et al.[24] in performing wind tunnel measurements on a modifiable leading edge aerofoil to improve dynamic stall characteristics during the blade motion.

Several attempts to model dynamic stall have been carried out in the CFD field during the last decades. Firstly, 2D Unsteady Reynolds-Averaged Navier Stokes (URANS) simulations of a pitching aerofoil are the most recurrent topic in the literature due to their cost-efficiency with respect to other approaches such as 3D URANS, Detached Eddy Simulation (DES) or Large Eddy Simulation (LES). Wang et al.[25] found that the SST k-ω model represents an improvement with respect to the standard k-ω. Both are precise in the linear lift range but fail to correctly predict the flow behaviour at high angles of attack and during the downstroke movement. Similar results were obtained by Honarmand et al.[26] who also showed the influence of the most relevant parameters in the dynamic stall utilizing 2D SST k-ω simulations. Nevertheless, Bangga et al.[27] recently obtained accurate force prediction with the 2D SST k-ω turbulence model.

K-ω SST has usually been found to be the most reliable turbulence model when considering dynamic stall. However, Bangga [28] revealed a better behaviour of the Spalart-Allmaras (SA) turbulence model in both static and dynamic cases, with better numerical results and prediction of the Leading Edge Vortex (LEV) breakdown.

Meanwhile, Gleize et al.[29] expressed the importance of considering transition modelling when solving cases at transitional Reynolds numbers. Wang et al.[30] also obtained better results using the Transition SST γ-Re_θ model with respect to the conventional SST model, which supposes a fully turbulent boundary layer.

It is widely known that RANS simulations struggle when calculating highly turbulent flow as the one around an aerofoil at stall conditions, especially when using a simplified 2D model. Because of this, multiple authors have tried to modify the turbulence model to adjust the flow behaviour to the experimental data. Chitsomboon et al.[31] stated that it is caused by the events occurring in the buffer zone of the boundary layer and proposed the addition of a damping function to limit the eddy viscosity in this region. This approach was followed for the study of the dynamic stall by Bangga et al.[32], with an enhancement on the phenomena prediction.

In addition, another more straightforward but still practical possibility can be implemented by changing the turbulence model coefficients. Zhang et al.[33] recently identified the most relevant parameters of the k-ω SST model, Zhong et al.[34] and Matyushenko et al.[35] concluded that this methodology decreases eddy viscosity and improves the prediction. However, the last ones also warned that modifying the coefficients destroys the calibration of the model, decreasing accuracy in simple turbulent flows.

On the 3D field, Khalifa et al.[36] demonstrated the higher precision of 3D URANS models with respect to 2D URANS, as well as the supremacy of Improved Delayed Detached Eddy Simulations (IDDES) to accurately predict flow behaviour against URANS cases due to its capability to resolve finer turbulence scales. Ferreira et al.[37] showed the importance of PIV data employing validation when simulating dynamic stall and the enhanced accuracy when using LES and DES compared to RANS.

Moreover, Abdulqadir et al.[38] studied the performance of URANS models with non-linear effective viscosity approximation. It was concluded that they are more precise than classical linear URANS models, which are not capable of returning the correct flow development at the considered operating range.

Though, Hand et al.[39] concluded quantitatively that URANS SA represents the best compromise between accuracy and computational requirement when compared to k-ω SST and DES. Similar conclusions were stated by Wang et al.[30], who did not observe an improvement in the prediction capability of the Delayed Detached Eddy Simulation (DDES) model with respect to 2D transitional models.

To sum up, multiple CFD approaches are available within the literature, and non-homogeneous conclusions have been stated on the best practices to model dynamic stall. What seems to be clear is that 2D URANS shows some limitations for predicting the flow behaviour at high angles of attack, while the most expensive methods as DES or LES seem to be more accurate. However, it is necessary to study the worthiness of 2D URANS simulations as they represent a much lower computational cost than scale-resolving approaches.

1.4 Dynamic Stall

This project aims to simulate and predict dynamic stall. Because of this, it is important to understand the characteristics of the phenomena. In this section, a physical explanation of the DS, the phases of the process, the most important parameters that influence it and classification into two different types of DS will be exposed.

Dynamic stall is a complex non-linear physical event that occurs in oscillating aerofoils when the angle of attack is increased rapidly beyond the static stall angle. According to McCroskey [13], the onset of DS can be delayed to incidences much larger than the static case, and it is characterized by the emergence of a large-scale dynamic stall vortex (DSV), which finally breaks down and causes more severe and persistent stall respect to the static one.

Due to this delay in the stall, aerodynamic forces and moments become larger than the static ones, and they present huge hysteresis with respect to the angle of attack. This has a big impact on the structural forces and aerodynamic efficiency.

The complexity of DS relies on the phenomena that can be involved in the process, such as flow separation, vortex formation or shear layer instability, as well as boundary layer laminar to turbulent transition at certain Reynolds numbers.

The development of the unsteady flow during one cycle of dynamic stall was classified into five different stages (Figure 1.4): *attached flow stage*, *stall development stage*, *stall onset*, *stalled stage* and *flow reattachment* [7].

At the beginning of the process, during the **attached flow stage** (a), the small angles of attack of the aerofoil allow the flow to stay attached to the surface. As in the static case, the increase in the incidence causes an increase in the lift coefficient at a similar rate in both cases. Increasing the angle of attack beyond the static stall one leads to a big recirculating flow zone at the suction side of the aerofoil (b). The **stall development stage** has started. However, as it can be seen in Figure 1.7, lift continues to increase above the maximum value for the static case but at a slightly lower rate than before because of the big reversal flow at the aerofoil.

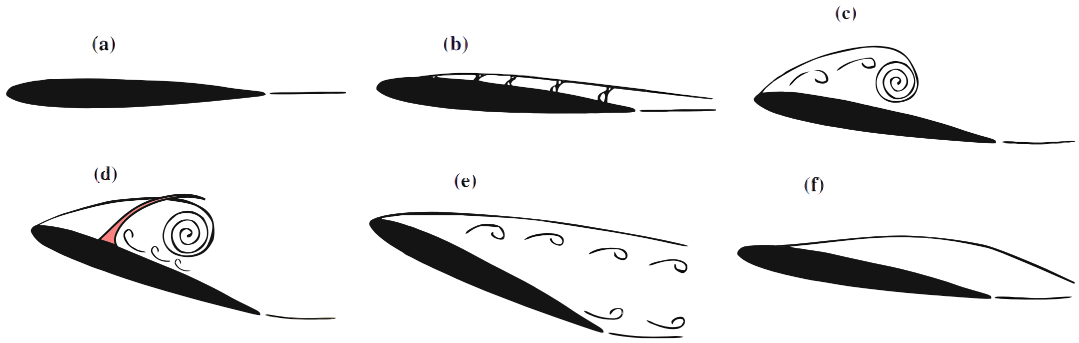

Fig. 1.4: Schematic representation of the different events of the dynamic stall process: (a) Attached flow, (b) Flow reversal, (c) Shear layer roll-up, (d) Stall onset, (e) Full stall, (f) Flow reattachment [2].

Due to the growth of the recirculating flow, a shear layer between it and the free stream flow is formed. A *primary instability* is developed, and as a result, small-scale vortexes detach and are pushed downstream. The interaction between vortices keeps increasing as the angle of attack does, resulting in a larger unattached flow region (*secondary instability*).

The coalescence of the small-scale vortex leads to the formation of a large-scale clockwise rotating vortical structure named primary dynamic stall vortex (PDSV), which corresponds with the shear layer roll-up event (c). During this later phase of the stall development stage, small-scale anticlockwise rotating induced vortices (IVs) are generated because of the interactions between the PDSV and the unattached flow. As visualized in Figure 1.5, these IVs are pushed to the leading edge of the aerofoil by the PDSV, which finally results in the separation of the PDSV and the start of the dynamic stall. Thus, this moment is named **stall onset** phase (d). It is characterized by a sudden change in the aerodynamic loads, specifically by a huge decrease in the aerofoil's lift (Figure 1.7).

The process of large-scale vortex formation and detachment is repeated during the downstroke movement of the aerofoil, which leads to high variations in the aerodynamic loads (see Figure 1.7), the main characteristic of the **stalled stage phase**.

Lastly, when the angle of attack is decreased enough, flow reattaches, and the aerodynamic loads converge to the initial value (**flow reattachment phase**).

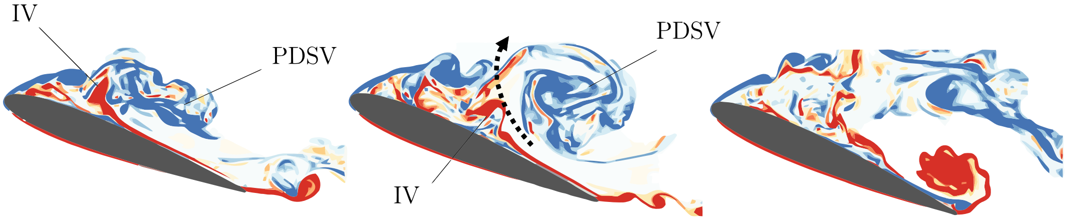

Fig. 1.5: Transition between the shear roll-up and the stall onset phases. In blue, clockwise vortices. In red, anticlockwise ones. Adapted from [6].

For a given aerofoil, McCroskey [13] defined two different **stall regimes** depending on the degree of flow separation present during the pitching of the aerofoil: *light stall* and *deep stall*. However, Mulleners et al.[7] proposed a more precise definition based on the moment of the dynamic stall vortex (DSV) detachment. If the DSV is expelled before the downstroke motion is initialized, it is called a deep stall regime, while if it is detached during the downstroke, it is a light stall.

Independently from this discrepancy, both state that the main parameter that influences the dynamic stall regime is the maximum angle of attack reached ($\alpha_m = \alpha_0 + \alpha_1$ for a sinusoidal motion). The larger this angle, the deeper the dynamic stall.

On the one hand, light stall regime occurs when the static stall angle is slightly exceeded and shares many features of a static stall, such as the classical lift drop, drag increase and negative (nose-down) pitching moment. As can be seen in Figure 1.6a, the unattached flow zone size is similar to the aerofoil thickness. However, the unsteady behaviour is present through force and flow attachment hysteresis.

On the other hand, deep stall happens when the static stall angle of attack is greatly overcome and is characterized by the vortex-shedding phenomena described previously. In this case, the thickness of the viscous layer is on the order of the chord (Figure 1.6b).

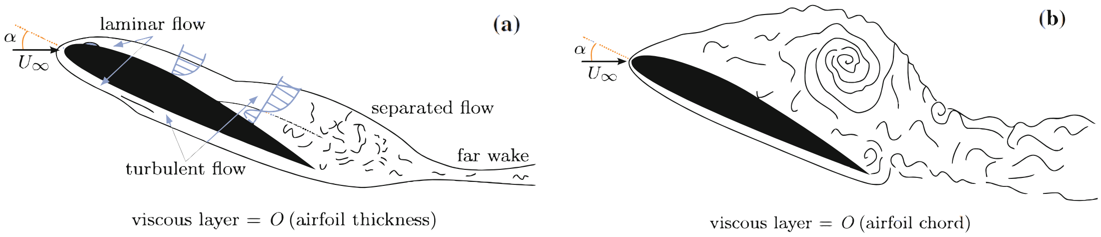

Fig. 1.6: On the left, light stall. On the right, deep stall scheme [7].

Moreover, differences between both cases in terms of lift can be seen in Figure 1.7. While the rate of growth of the lift with the angle of attack is similar in both cases, in the deep stall, the maximum lift coefficient is larger. As well as this, the force drop in the deep stall is significantly bigger, with higher oscillations during the downstroke motion.

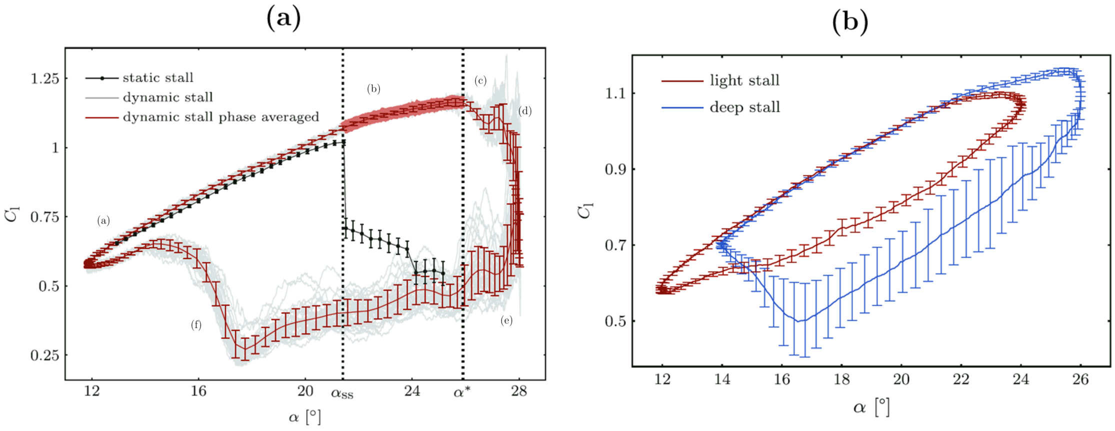

Fig. 1.7: On the left, comparison between lift coefficient in static and dynamic stall [7]. On the right, comparison between lift coefficient in light and deep dynamic stall [2].

Opposite to the static case, where the flow field rapidly changes when changing the angle of attack, the dynamic stall case is characterized by the lag between the motion of the body and the flow response. Because of this, although the instantaneous angle of attack is still important in the phenomena, it is not the only critical parameter in the DS.

One of the main complexities of analyzing and modelling the dynamic stall phenomena is its dependence on multiple parameters [13]:

- **Geometry**. One of the most important parameters, especially in the light stall regime, is the leading edge geometry. As in the static case, the sharper the LE, the abrupter the stall. As it can be seen in Figure 1.8, in thin aerofoils, there is a more sudden development of the dynamic stall vortex, while in thick aerofoils like the NACA0018, the stall starts from the trailing edge and growth towards the LE before the DSV development.
- **Reduced frequency**. The effect of the frequency of oscillation in the DS is highly dependent on the stall regime and the type of boundary layer separation. Generally, as it is increased, the maximum lift coefficient and hysteresis loop also do.
- **Amplitude and Mean angle**. As it has been said before, amplitude and mean angle mainly influence the type of stall regime through the maximum incidence (Figure 1.7b).

- **Mach number**. For low Mach number flows, the influence of this parameter is negligible. However, as flow velocity increases, its influence becomes larger, especially near sonic conditions where shock waves appear.
- **Other parameters**. Other factors such as the type of motion (sinusoidal, plunge, linear swept) or possible 3D effects produced by flow interaction or geometry (e.g. sweep) also can influence the dynamic stall development.

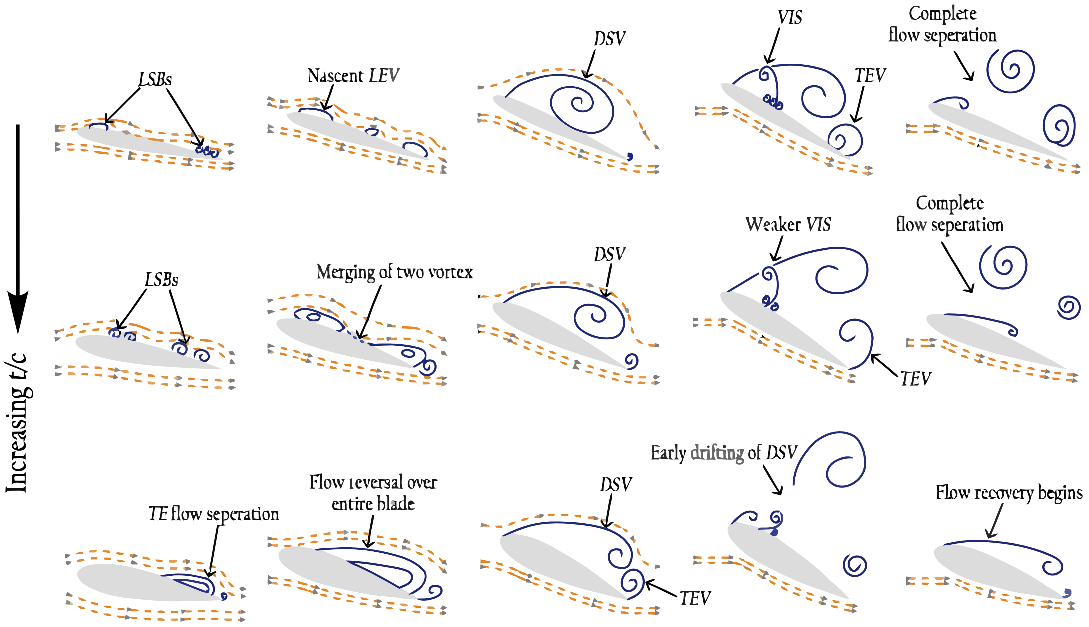
LSBs
Nascent LEV
DSV
VIS
Complete flow seperation
TEV
Increasing t/c
LSBs
Merging of two vortex
DSV
Weaker VIS
Complete flow seperation
TEV
TE flow seperation
Flow reversal over entire blade
DSV
TEV
Early drifting of DSV
Flow recovery begins

Fig. 1.8: Dynamic stall development depending on the aerofoil relative thickness [8].

1.5 Turbulence modelling

As was explained before, dynamic stall is a highly unsteady and non-linear phenomenon characterized by a large amount of turbulent flow. Moreover, turbulence modelling is one of the most critical aspects of the CFD to achieve reliable results as it is the main source of model uncertainty [9] and a relevant aspect of the computational cost. Thus, a good understanding of the turbulence resolving possibilities is highly relevant in this project.

Turbulent flows are characterized by a wide variety of spatial and temporal scales. Thus, considering the whole Navier-Stokes equations and solving all these scales, what is known as Direct Numerical Solving (DNS), is unaffordable because of its high computational cost, specially at high Reynolds numbers.

Reynolds Averaged Navier-Stokes (RANS) approach aims to solve this problem by modelling the entire range of temporal and spatial turbulent scales. However, not directly resolving the turbulent flow leads to a loss of fidelity and solution uncertainty, which will vary depending on the studied case. Several well-known RANS turbulence models have been developed in the last decades, such as k-ϵ, k-ω, k-ω SST, Spalart-Allmaras etc.

Large Eddy Simulation (LES) represents a trade-off between RANS and DNS, solving the larger scales, which are the most energetic ones, and modelling the smaller ones between a certain filter threshold. In this way, the LES approach obtains a more faithful solution than in the RANS case, with a significantly lower cost compared to DNS but still too high for most industrial applications.

Because of this, as it is shown in Figure 1.9a, a hybrid approach between LES and RANS is possible, called Detached Eddy Simulation (DES). This kind of turbulence treatment uses the RANS treatment near the wall and switches on the LES treatment in detached regions, reducing the computational cost significantly but still offering the precision of LES in turbulent flows.

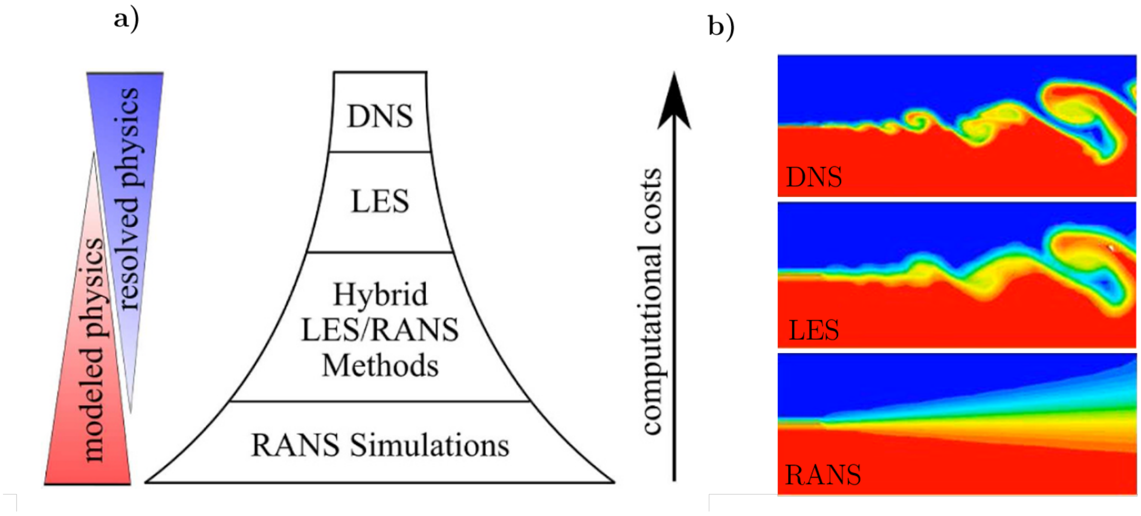

Fig. 1.9: At left, scheme of the different turbulence modelling approaches [9]. At right, example of solution using DNS, LES and RANS [10].

In Figure 1.9b, it can be seen a comparison between three different solutions for the same case using DNS, LES and RANS. As predictable, the detailed turbulence solution obtained in the DNS case is not comparable to the one obtained by RANS. Thus, if a high resolution of spatial and temporal scale is desired, one should choose a high fidelity approach.

In this project, mainly the RANS approach will be considered because of being the most computationally affordable. Different turbulence models will be tested, and results will be compared to the experimental case to choose the one which better fits the trade-off between cost and precision.

Chapter 2

Methods

This chapter will explain the whole process of simulating the NACA0018 aerofoil under dynamic stall using OpenFOAM. Firstly, a case description will be presented, defining the fundamental parameters that control the aerofoil movement. Then, the most relevant parts of the CFD process will be exposed: conceptual modelling, geometry and domain, boundary conditions, meshing, solvers and turbulence modelling.

2.1 Case description

As stated in Section 1.4, several parameters influence the dynamic stall behaviour of an aerofoil. The movement-related ones are the type of motion, mean angle, α_0, angle amplitude, α_1, and reduced frequency ,k. For this project, a simple sinusoidal motion will be considered,

$$\alpha(t) = \alpha_0 + \alpha_1 \sin(\omega t) \tag{2.1}$$

where ω is the angular velocity.

In addition, reduced frequency is defined as

$$k = \frac{c\pi f}{U_\infty} \qquad\qquad \omega = 2\pi f \tag{2.2}$$

where c is the aerofoil's chord, U_∞ is the free stream velocity and f the motion's frequency.

A parametric study will be performed to study the influence of the three main variables in the dynamic stall. As it can be seen in Table 2.1, the influence of reduced frequency, amplitude and turbulence intensity will be studied.

Study	$Re \cdot 10^5$ [-]	TI [%]	α_0 [deg]	α_1 [deg]	f [Hz]	k [-]
1	3	0.05	14	10	0.4	0.025
		0.05		10	1	0.063
		0.05		10	1.6	0.1
2	3	0.05	14	6	1	0.063
		0.05		8	1	0.063
		0.05		10	1	0.063
		0.05		14	1	0.063
3	3	0.05	14	14	1	0.063
		0.5		14	1	0.063
		3		14	1	0.063
		7.5		14	1	0.063

Table 2.1: Parametric studies considered in this project.

A comparison between these movements is shown in Figure 2.1. Obviously, increasing the movement amplitude will lead to a higher maximum angle of attack α_m, which is a crucial aspect of the dynamic stall regime determination (deep stall, light stall). Moreover, suppose the frequency is kept constant. In that case, it will also increase the angular velocity $\dot{\alpha}(t)$ for a certain instantaneous angle, as the aerofoil must cover a wider range within the same period. On the other hand, a more significant reduced frequency will also increase the angular velocity and reduce the motion's period.

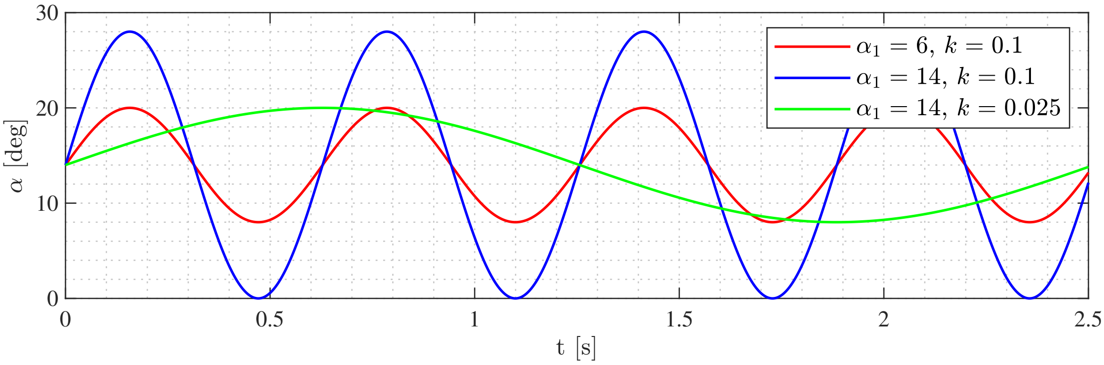

Fig. 2.1: Influence of reduced frequency and amplitude in the aerofoil's motion.

Lastly, in Table 2.2 fluid properties are shown. Fluid considered is air, with $\rho = 1.2$ kg/m^3 and $\mu = 1.8 \cdot 10^{-5}$ Pa $\cdot$ s. The aerofoil's chord is $c = 0.3$ m and the far field velocity is $U_\infty = 15$ m/s, which leads to $Re = 3 \cdot 10^5$.

Re [-]	c [m]	U_∞ [m/s]	ρ [kg/m^3]	μ [Pa $\cdot$ s]
$3 \cdot 10^5$	0.3	15	1.2	$1.8 \cdot 10^{-5}$

Table 2.2: Fluid and flow properties used to simulate dynamic stall.

2.2 Conceptual modelling

This part of the CFD process is about establishing the study objectives and determining the possible simplifications (e.g. steady, symmetry) that can be applied depending on the desired precision and the available computational capabilities. In this case, steady simplifications can not be applied due to the dynamic stall unsteadiness. Moreover, no symmetry planes can be defined. Nevertheless, the incompressible simplification will be considered as the flow around the aerofoil is air at a Mach number much lower than $M = 0.3$.

On the other hand, 2D simplification is usually taken by authors in the available literature. It is widely known that turbulence implies 3D effects, leading to non-accurate results, especially in the deep stall region, if the 2D assumption is considered. However, solving a 3D unsteady case can be prohibitively expensive in most cases. That is why the 2D approach is worth trying, significantly reducing the computational cost while maintaining reasonable accuracy.

Thus, this project will compare the results between 2D and 3D cases, looking for a compromise between accuracy and affordability. It is important to remark that this project is developed in an MSc thesis context, so precision is accepted to be lower than in an industrial environment.

2.3 Geometry, domain and boundary conditions

Regarding the domain of the CFD case, in Figure 2.2a, a conceptual scheme of the case can be seen, and in Figure 2.2b, the used domain is shown. Firstly, an O-shape mesh allows for easily rotating the whole domain without the presence of interface regions that may produce a higher computational cost and uncertainty. The geometry is produced using the software *Pointwise* [40].

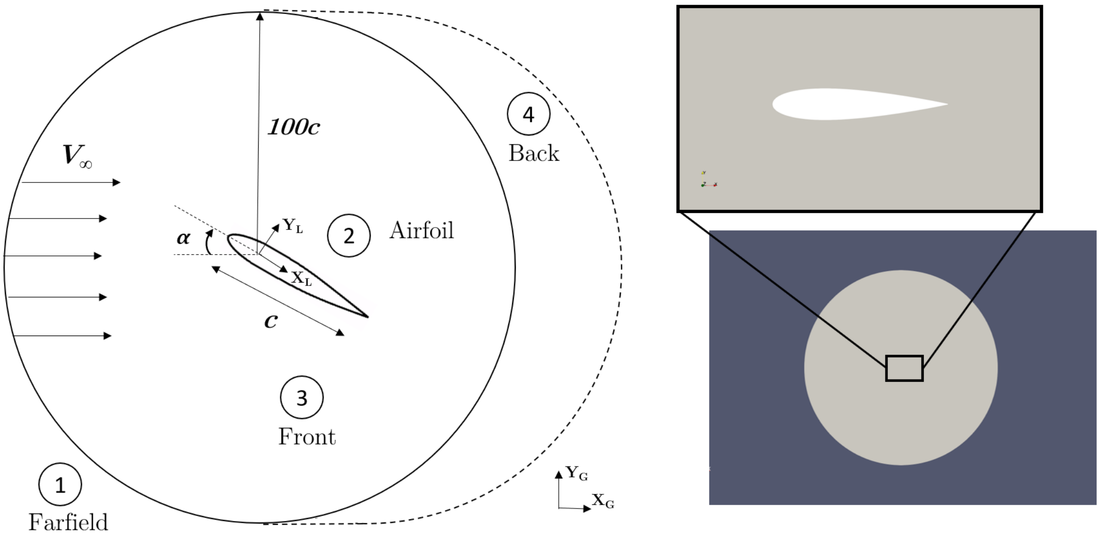

a)

b)

Fig. 2.2: On the left, a conceptual scheme of the considered domain. On the right, the O-shape domain with a close-up of the NACA0018 at the centre.

Besides, the domain radius, $R = 100c$, was set large enough to correctly solve the flow downstream of the aerofoil and avoid convergence problems while keeping a good prediction of the air loads. The velocity inlet is kept constant in the global X-axis direction, X_G, while the entire domain rotates with respect to the aerofoil's aerodynamic centre, $X_{AC} = 0.25c$. In this way, an instantaneous angle of attack, α, is created between the aerofoil and the incoming flow. Moreover, in the 3D case, the aerofoil's span is defined as $w = 0.2$ m.

Moreover, four patches compose the domain: *farfield*, *aerofoil*, *back* and *front*. The specific boundary conditions (BC) used in OpenFOAM regarding pressure and velocity are shown in Table 2.3.

Domain patch	Pressure (p)	Velocity (U)
Farfield	freestreamPressure	freestreamVelocity
Aerofoil	zeroGradient	movingWallVelocity
Front (2D / 3D)	empty / symmetryPlane	empty / symmetryPlane
Back (2D / 3D)	empty / symmetryPlane	empty / symmetryPlane

Table 2.3: Pressure and Velocity boundary conditions in each patch for the 2D and 3D cases.

A velocity inlet is imposed in the inlet and a pressure outlet in the outlet utilising the *freestream* BC at the far-field patch. It calculates the mass flow rate, and if the flow is going outside, the boundary will be locally *zeroGradient*; if it is going inside, the boundary will be locally *fixedValue*. Thus, it allows a velocity inlet and pressure outlet within the same patch.

On the other hand, regarding the aerofoil patch, a *zeroGradient* pressure and *movingWallVelocity* set the no-slip condition on the aerofoil walls. In the 2D case, back and front patches are defined as empty, while in the 3D case, they are set to *symmetryPlane*. Lastly, the turbulence boundary conditions will be presented in Section 2.6.

2.4 Meshing

The meshing step is one of the most relevant in a CFD process. Firstly, it determines a significant part of the computational cost. Besides, the mesh quality sets the solving accuracy and the convergence rate of the case. Thus, it is crucial to have a good quality mesh and perform the necessary mesh independence studies.

In this project, a structured mesh using the software *Pointwise* [40] has been built to keep a high mesh quality and reduce the computational cost and numerical error. The final mesh is shown in Figure 2.3. The mesh was built to keep a wall $y^+ < 1$ in the whole surface as low-Re turbulence models will be used,

$$y^+ = \frac{y_1 u_\tau}{\nu} \qquad\qquad u_\tau = \sqrt{\frac{\tau_w}{\rho}} = \sqrt{0.5 c_f u_\infty^2} \tag{2.3}$$

where y_1 is the first cell size, ν is the kinematic viscosity and c_f is the friction coefficient.

Number of cells [-]	y_1 [m]	GR [-]	Aerofoil points [-]
37125	$2.5 \cdot 10^{-5}$	1.1	300

Table 2.4: Parameters of the final structured mesh.

Moreover, data regarding this mesh is shown in Table 2.4, with *GR* the growth ratio of the mesh. The mesh has a maximum skewness of 1.72 and an average and maximum non-orthogonality of 0.61 and 18.48, respectively. The maximum aspect ratio is 101.2 near the aerofoil to capture the large gradients in this zone adequately. Besides, Figure 2.4 shows the wall y^+ at different angles of attack. The value is below 1 on most aerofoil surface, except for a small part near the leading edge.

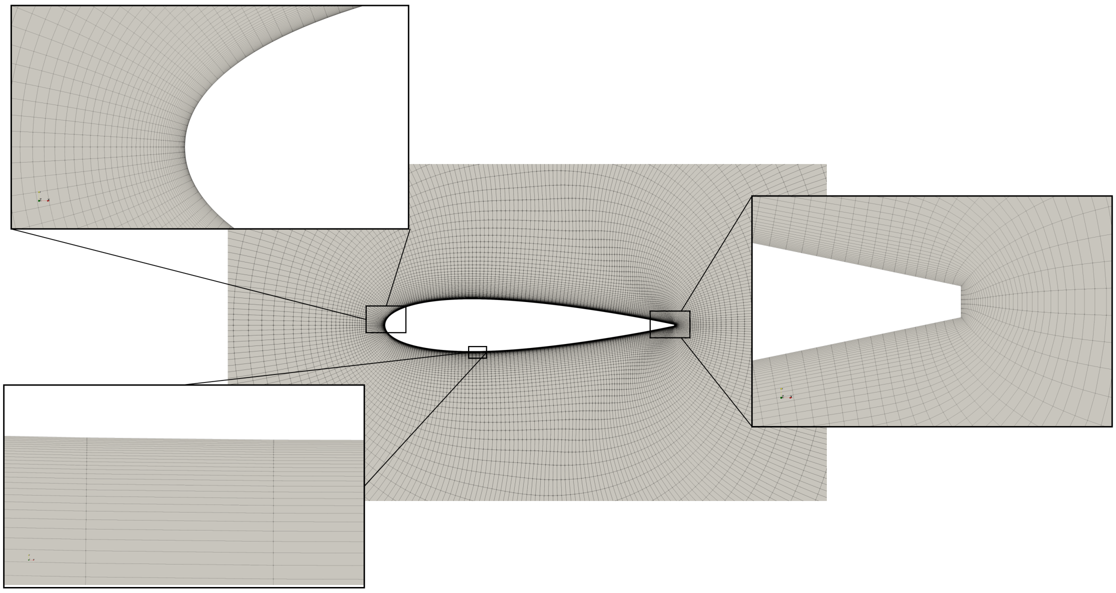

Fig. 2.3: Final mesh generated with *Pointwise* with close-ups to the leading edge, trailing edge and the boundary layer (wall $y^+ < 1$).

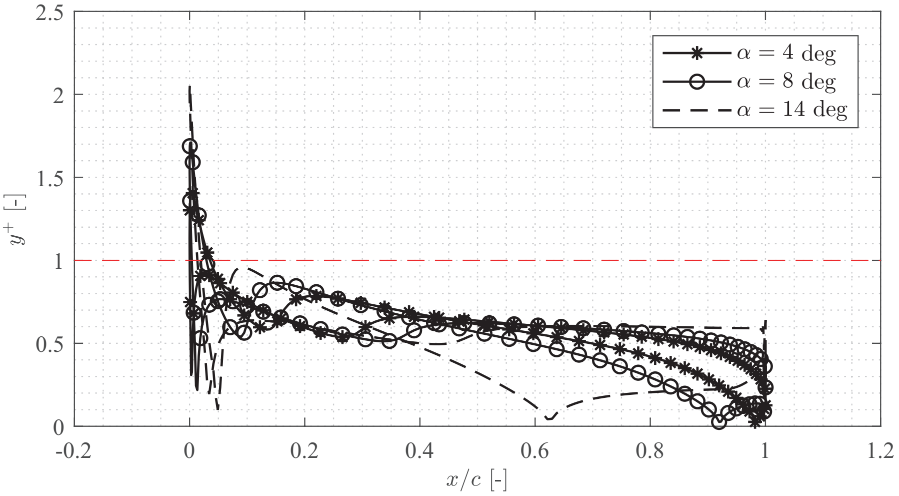

Fig. 2.4: Wall y^+ through the aerofoil's surface for different angles of attack α in static cases.

On the other hand, a mesh independence study has been performed to ensure an acceptable accuracy with the minor possible computational cost. For this, two different steps have been applied. Firstly, a generalisation of Richardson's Extrapolation has been considered to choose the growth ratio. Then, a sensibility study of the aerofoil's points variable was done.

Richardson's Extrapolation

Richardson's Extrapolation is recognised as a complete and correct methodology to study the mesh independence [41]. The basic idea is to fit a function to the cell length (h) and variable of interest (in this case c_l) data. This function can be used to extrapolate the variable's value when $h = 0$ m, i.e., the solution with no spatial discretization error.

An ideal CFD calculation is second-order accurate. Thus, the order of convergence p is 2, i.e., the variable varies in proportion to h^2. In practice, this is not true, and the value of p is lower than 2. The general shape of the Richardson's Extrapolation is

$$C_L = C_{L0} + c_{re} \cdot h^p \tag{2.4}$$

where c_{re}, C_{L0} and p are unknown constants that must be solved.

There are three unknowns; at least three solutions for different cell lengths are needed (equations). Thus, *fine* (1), *medium* (2) and *coarse* (3) meshes will be used for the study. Once the solution is obtained for each mesh, the value of the three unknowns will be calculated with a bisection method using the following equations,

$$c_{re} = \frac{C_{L1} - C_{L0}}{h_1^p}, \quad C_{L0} = \frac{r_{21}^p \cdot C_{L1} - C_{L2}}{r_{21}^p - 1};$$

$$p = \frac{1}{\ln r_{21}} \left| \ln \left| \frac{\epsilon_{32}}{\epsilon_{21}} \right| + \ln \left(\frac{r_{21}^p - 1}{r_{32}^p - 1} \right) \right|; \tag{2.5}$$

$$\epsilon_{ij} = C_{Li} - C_{Lj}, \qquad r_{ij} = h_i/h_j.$$

Regarding the discretisation error estimation, three different definitions of it are used. First of all, the relative error, e_{21}, is the standard method used to evaluate the discretisation error. Secondly, the extrapolated relative error, which is the deviation between the solution and calculated value of zero discretisation error e_{02}^e. Lastly, the Grid Convergence Index, GCI_{21}, also takes into account the order of convergence p. In this case, a safety factor of 1.25 is used. Formulas for the three errors are

$$e_{21} = \left| \frac{C_{L2} - C_{L1}}{C_{L1}} \right| \qquad e_{21}^e = \left| \frac{C_{L1} - C_{L0}}{C_{L0}} \right| \qquad GCI_{21} = \frac{1.25 e_{21}}{r^p - 1}. \tag{2.6}$$

The data of the three meshes used in this project for Richardson's Extrapolation is shown in Table 2.5, where h represents the average cell size of the cell elements, calculated as

$$h = \frac{1}{N_y} \cdot \sum_{i=0}^{N_y - 1} y_1 \cdot (GR)^i \tag{2.7}$$

with N_y being the number of consecutive cells in the y direction.

A comparison between two meshes of this study is shown in Figure 2.5. As the GR is lower in Mesh 1, the number of elements close to the aerofoil significantly increases.

Case	Number of cells [-]	h [m]	GR [-]	Aerofoil points [-]
Mesh 3	26196	0.25	1.10	400
Mesh 2	58064	0.20	1.08	400
Mesh 1	103878	0.15	1.06	400

Table 2.5: Parameters of the meshes considered for the Richardson's Extrapolation study.

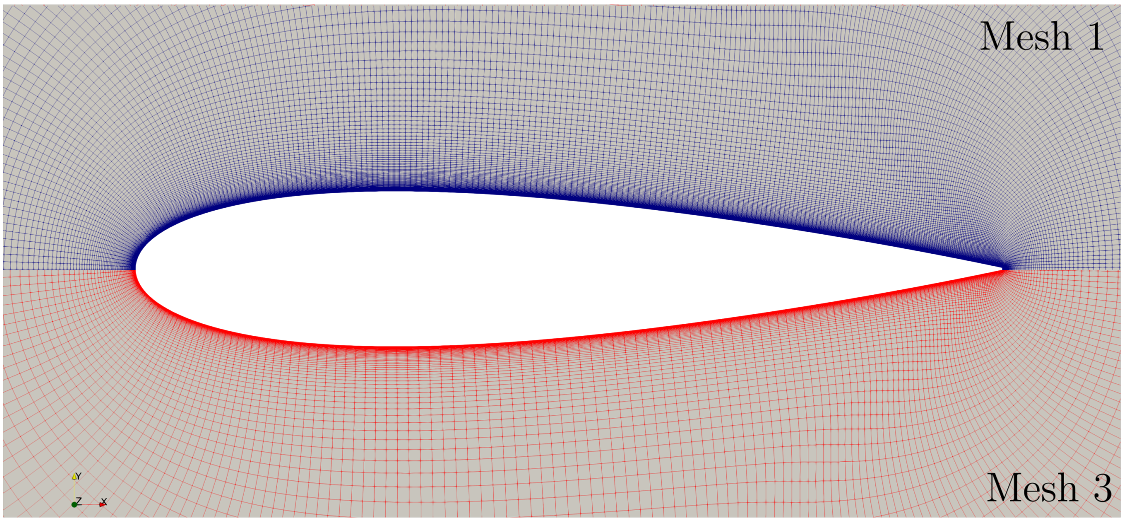

Fig. 2.5: Above, Mesh 1 with $GR = 1.1$ and $N = 26196$. Below, Mesh 3 with $GR = 1.06$ and $N = 103878$.

Results for the three meshes and three different angles of attack with Richardson's Extrapolation parameters and errors defined previously can be seen at Table 2.6 and the error evolution with the angle of attack for the medium and fine meshes is shown in Figure 2.6a. An example to illustrate the method application at $\alpha = 12$ deg is shown in Figure 2.6b. It can be seen that the solution tends asymptotically to the value without discretisation error.

α [deg]	r_{21} [-]	r_{32} [-]	p [-]	C_{L0} [-]	e_{21} [%]	e^e_{01} [%]	e^e_{02} [%]	GCI_{21} [%]
6	1.35	1.25	1.75	0.591	0.03	0.36	0.40	0.08
12	1.35	1.25	1.53	1.077	0.35	0.60	0.95	1.09
16	1.35	1.25	1.88	1.171	1.51	1.17	2.69	3.63

Table 2.6: Results for the coarse, medium and fine mesh at different angles of attack with the Richardson's Extrapolation parameters calculated.

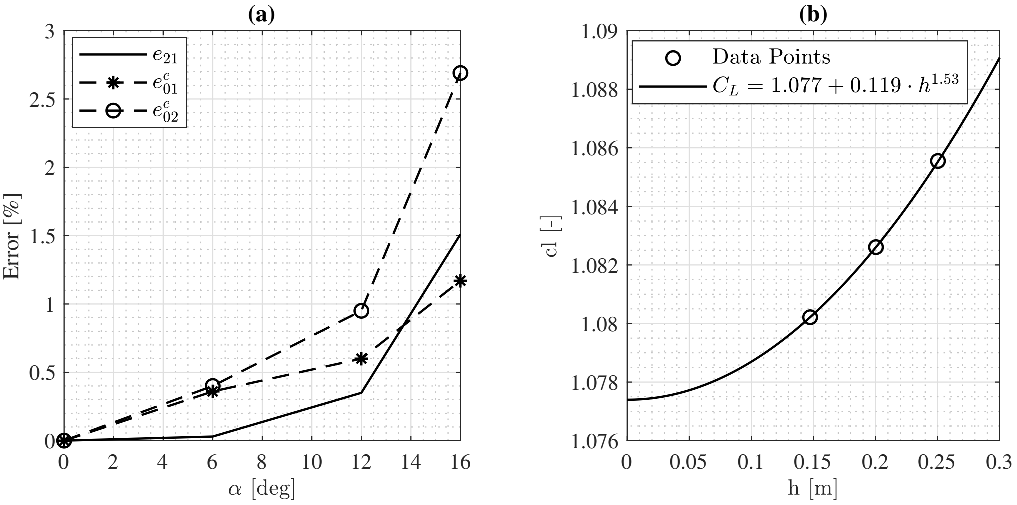

Fig. 2.6: At the left, relative and extrapolated error of the fine and medium meshes. At the right, example of application of the Richardson's Extrapolation for $\alpha = 12$ deg.

For $\alpha = 6$ deg and $\alpha = 12$ deg all the errors are below 1%. In the higher incidence case, the relative error goes up to 1.51%, and the extrapolated error of the medium mesh is 2.69%. As stated before, the project's scope is within an MSc thesis, so this discretisation error is completely acceptable. Furthermore, as can also be seen in Figure 2.7, the computational cost of the medium mesh is half the one of the finer mesh. Thus, the medium mesh is decided to be the best in this case.

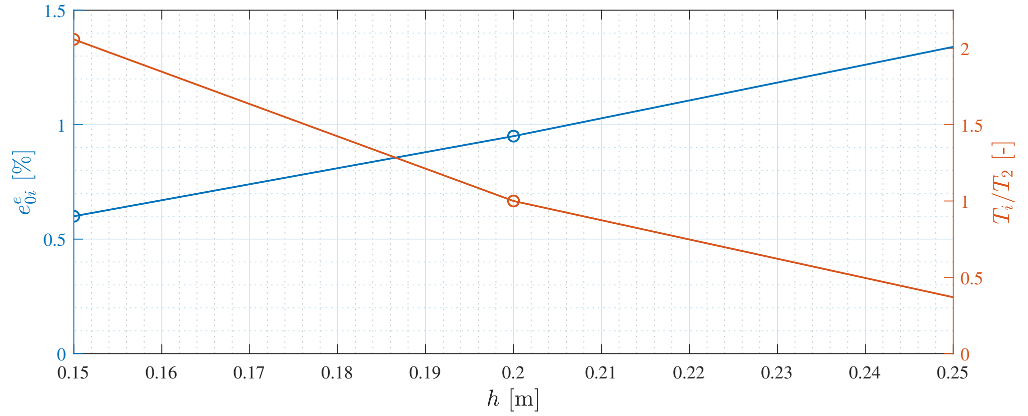

Fig. 2.7: In blue, extrapolated error for the coarse ($h = 0.25$ m), medium ($h = 0.20$ m) and fine ($h = 0.15$ m) meshes. In orange, dimensionless computational time respect to the medium mesh time.

Aerofoil Points study

The second step of the mesh independence study was to study the solution sensibility to the number of points on the aerofoil's surface. The data of the tested meshes are shown in the Table 2.7, and a comparison between two different meshes of the study is shown in Figure 2.8. As stated before, Mesh 2 is considered the best of the previous case. Thus, it is also taken into account in this study. The growth ratio between the meshes is also changed to preserve a proper cell aspect ratio near the aerofoil's surface.

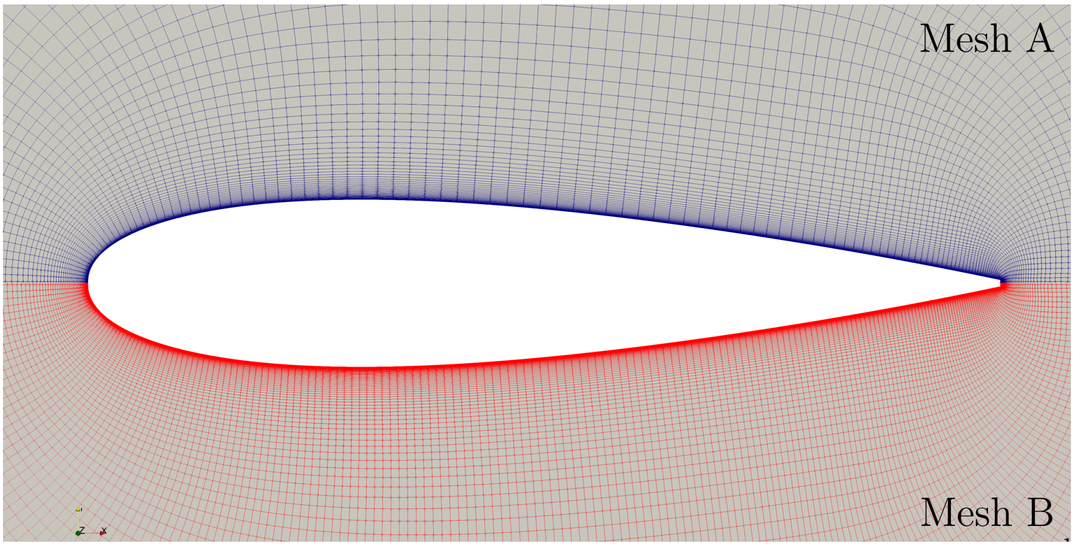

Fig. 2.8: Above, Mesh A with $GR = 1.06$ and 500 Aerofoil Points. Below, Mesh B with $GR = 1.1$ and 300 Aerofoil Points.

Case	Number of cells [-]	GR [-]	Aerofoil points [-]
Mesh A	96418	1.06	500
Mesh B	37125	1.10	300
Mesh C	21079	1.12	200
Mesh 2	58064	1.08	400

Table 2.7: Meshing parameters considered for the Aerofoil Points study.

Results regarding the study are shown in Figure 2.9. As it can be seen in (a), results from meshes B and C do not differ significantly from the Mesh 2 ($e_{i2} < 1\%$). Only the Mesh A at the most significant incidence shows a notable difference. On the other hand, by (b), Mesh B gives similar results with respect to Mesh 2 and has almost half of the elements. Thus, the computational cost associated with Mesh B will be considerably lower. Although Mesh A is more accurate than Mesh B, the difference is not high until $\alpha = 16$ deg, with a reduction of a 1.5% in error. Besides, Mesh C has one third the number of elements of Mesh A, thus being much more affordable to solve.

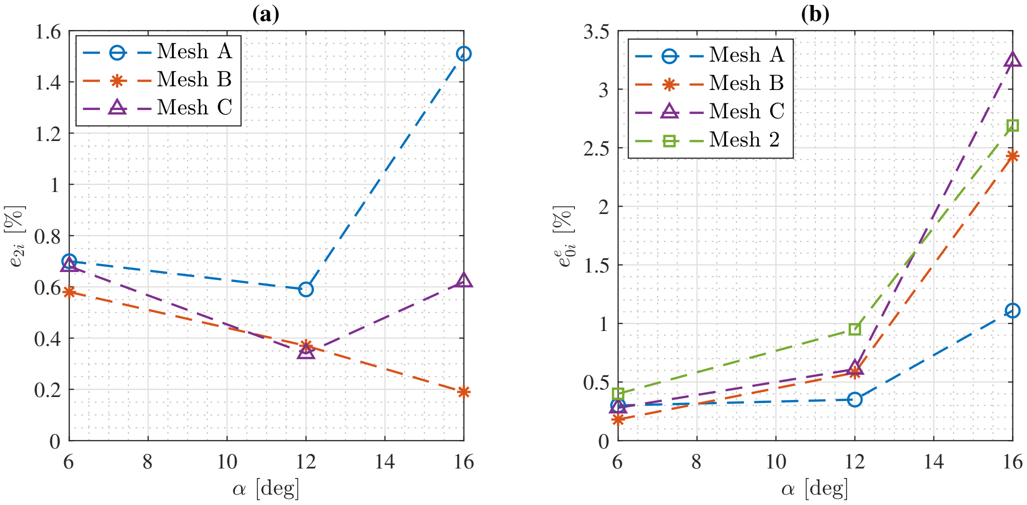

Fig. 2.9: At the left, relative error of the tested meshes respect to the Mesh 2. At the right, extrapolated relative error of the four meshes.

The project's objective is to study the dynamic stall of a pitching aerofoil, which involves running unsteady simulations that are known to be significantly costly. Thus, **it is decided to use the Mesh B**, as it shows an excellent trade-off between accuracy and computational cost.

Finally, it is important to remark that the 3D mesh has been constructed by extruding Mesh B through the 0.2 metre span with 16 cells in the Z-direction. Thus, a 594000 cells mesh is used for the three-dimensional cases.

2.5 Solver setup

Unsteady simulations are launched to solve the dynamic stall of the pitching NACA0018. Besides, static cases are launched for the mesh independence studies and initialising the unsteady cases. Both the steady and unsteady setups are shown in this section.

The Semi-Implicit Method for Pressure Linked Equations (SIMPLE) algorithm is used for the steady case. In OpenFOAM it is known as *simpleFOAM*. Solvers employed to carry out the simulations are shown in Table 2.8.

Equation	p	$pcorr$	U	k	ω
Solver	GAMG	GAMG	smoothSolver	smoothSolver	smoothSolver
Smoother	GaussSeidel				

Table 2.8: Solver and smoother used for each equation at the steady case.

For the unsteady case, the Pressure-Implicit with Splitting of Operators (PISO) algorithm is used, which is set in OpenFOAM using the *pimpleFOAM* solver with $nOuterCorrectors = 1$. The Courant-Friedrichs-Levy Number (C) has been kept below 5 in the slow sweep cases and below 1 in the fast ones to ensure numerical stability and precision while reducing the computational cost. Solvers used for the unsteady simulations are shown in Table 2.9.

Equation	p	$pFinal$	$pcorr$	U	$UFinal$	k	$kFinal$	ω	$\omega Final$
Solver	PCG			smoothSolver					
Preconditioner	DIC			GaussSeidel					

Table 2.9: Solver and preconditioner used for each equation at the unsteady case.

Lastly, discretisation schemes for both the steady and unsteady cases used are presented in Table 2.10. As it can be seen, the second-order scheme is not used in the *omega* variable of the divergence term. This is because of numerical instability within the high turbulence region. Thus, a trade-off between precision and stability has been searched.

Term	Scheme
Time	CrankNicolson 0.7
Gradient	Cell limited Gauss linear
Divergence	Gauss linearUpwind / upwind
Laplacian	Gauss linear
Interpolation	Linear
snGradient	Limited

Table 2.10: Discretization schemes used for both the steady and unsteady cases.

2.6 Turbulence modelling

As it has been stated in Section 1.5, the RANS approach will be considered to model the turbulence behaviour. In this way, three different turbulence models will be tested: Spalart-Allmaras (SA), k-ω Shear Stress Transport (SST) and Langtry-Menter k-ω Shear Stress Transport (SST). Besides, static DES k-ω SST cases will also be launched to compare the results with the RANS simulations. This section presents a brief description of the turbulence models and the initial conditions used for the turbulent parameters in each of them.

Spalart-Allmaras (SA)

The Spalart-Allmaras turbulence model [42] was developed for the aerospace industry. It is known to model properly flows around aerofoils subjected to adverse pressure gradients. SA has the advantage of lower computational cost with respect to other turbulence models. It is a one equation model that solves the kinematic turbulent viscosity, μ_t, by the estimation of a modified turbulence viscosity, $\bar{\nu}$,

$$\frac{D}{Dt}(\rho\bar{\nu}) = \nabla\cdot(\rho D_{\bar{\nu}}\bar{\nu}) + \frac{C_{b2}}{\sigma_{\nu_t}}\rho|\nabla\bar{\nu}|^2 + C_{b1}\rho\bar{S}\bar{\nu}\,(1-f_{t2}) - \left(C_{w1}f_w - \frac{C_{b1}}{\kappa^2}f_{t2}\right)\rho\frac{\bar{\nu}^2}{\bar{d}^2} + S_{\bar{\nu}}. \quad (2.8)$$

Initial conditions used for this turbulence model are presented in Table 2.11. Modified Turbulence Viscosity values are set based on [43].

Domain patch	Modified Turbulence Viscosity (nuTilda)	
	Type	Value
Farfield	inletOutlet	$6 \cdot 10^{-5}$
Aerofoil	fixedValue	0
Front (2D / 3D)	empty / symmetryPlane	
Back (2D / 3D)	empty / symmetryPlane	

Table 2.11: Initial conditions used for the Spalart-Allmaras cases.

k-ω Shear Stress Transport (SST)

The k-ω Shear Stress Transport (SST) [44] two equation turbulence model is one of the most used due to its adaptability to different applications,

$$\frac{D}{Dt}(\rho\omega) = \nabla \cdot (\rho D_\omega \nabla\omega) + \rho\gamma\frac{G}{\nu} - \frac{2}{3}\rho\gamma\omega(\nabla \cdot \mathbf{u}) - \rho\beta\omega^2 - \rho\left(F_1 - 1\right)CD_{k\omega} + S_\omega, \quad (2.9)$$

$$\frac{D}{Dt}(\rho k) = \nabla \cdot (\rho D_k \nabla k) + \rho G - \frac{2}{3}\rho k(\nabla \cdot \mathbf{u}) - \rho\beta^*\omega k + S_k. \quad (2.10)$$

It combines the accuracy of the standard k-ω in the near-wall zone and the robustness of the k-ϵ away from it. Besides, it incorporates a turbulent production limiter to avoid too high turbulent kinetic energy production in stagnation zones. It is known to give reliable results for flow near aerofoils, as in the case of dynamic stall.

Initial conditions used for this turbulence model are presented in Table 2.12. The initial conditions are chosen based on literature [45], except the turbulence kinetic energy (TKE) value at far-field, which is calculated from the turbulence intensity (TI) with

$$TKE = \frac{3}{2} \cdot \left(TI \cdot U_\infty\right)^2. \quad (2.11)$$

Furthermore, static DES cases will be calculated. As explained before, the DES approach combines LES resolution far from walls and RANS near them to find a compromise between accuracy and computational cost. Thus, the definition of the filter width (Δ) for the LES case is needed. In this project, a cube-root volume delta is used, as it is appropriate for isotropic hexahedral meshes,

$$\Delta = c_{LES}\left(V_c\right)^{\frac{1}{3}}. \quad (2.12)$$

with V_c being the cell volume and c_{LES} a constant.

Domain patch	TKE (k)		Rate of Dissipation (omega)	
	Type	Value	Type	Value
Farfield	inletOutlet	$8.43 \cdot 10^{-5}$	inletOutlet	2.5
Aerofoil	fixedValue	0	fixedValue	$7.68 \cdot 10^{7}$
Front (2D / 3D)	empty / symmetryPlane		empty / symmetryPlane	
Back (2D / 3D)	empty / symmetryPlane		empty / symmetryPlane	

Table 2.12: Initial conditions used for the k-ω SST cases.

Langtry-Menter k-ω Shear Stress Transport (SST)

The transition SST k-ω model [46], also called γ- Re_θ, is a four equation model that aims to predict the laminar to turbulent boundary layer transition in medium Reynolds number flows. It incorporates two extra equations to solve γ and Re_θ,

$$\frac{\partial(\rho\gamma)}{\partial t} + \frac{\partial\left(\rho u_j \gamma\right)}{\partial x_j} = P_\gamma - E_\gamma + \frac{\partial}{\partial x_j}\left[\left(\mu + \frac{\mu_t}{\sigma_f}\right)\frac{\partial\gamma}{\partial x_j}\right], \tag{2.13}$$

$$\frac{\partial\left(\rho\hat{Re}_{\theta t}\right)}{\partial t} + \frac{\partial\left(\rho u_j \hat{Re}_{\theta t}\right)}{\partial x_j} = P_{\theta t} + \frac{\partial}{\partial x_j}\left[\sigma_{\theta t}\left(\mu + \mu_t\right)\frac{\partial \hat{Re}_{\theta t}}{\partial x_j}\right]. \tag{2.14}$$

Initial conditions used for this turbulence model are presented in Table 2.12 and Table 2.13. The initial conditions are chosen based on literature [47].

Domain patch	Intermittency (gammaInt)		Transition momentum thickness Reynolds number (ReThetat)	
	Type	Value	Type	Value
Farfield	inletOutlet	1	inletOutlet	880
Aerofoil	zeroGradient	-	zeroGradient	-
Front (2D / 3D)	empty / symmetryPlane		empty / symmetryPlane	
Back (2D / 3D)	empty / symmetryPlane		empty / symmetryPlane	

Table 2.13: Initial conditions used for the Langtry-Menter k-ω SST cases.

2.7 Convergence criteria

Lastly, defining the convergence criteria for the CFD simulation is a crucial aspect of the process. In this project, a double check in the convergence will be used.

On the one hand, residuals will be looked at (Figure 2.10a). For the static cases, a value under 10^{-5} is considered the convergence threshold. In the dynamic cases, a more permissive criterion is used ($p < 10^{-3}$ and $\{U_x, U_y, k, \omega\} < 10^{-5}$) due to the unsteady nature of the cases, which can lead to significant variations during the process.

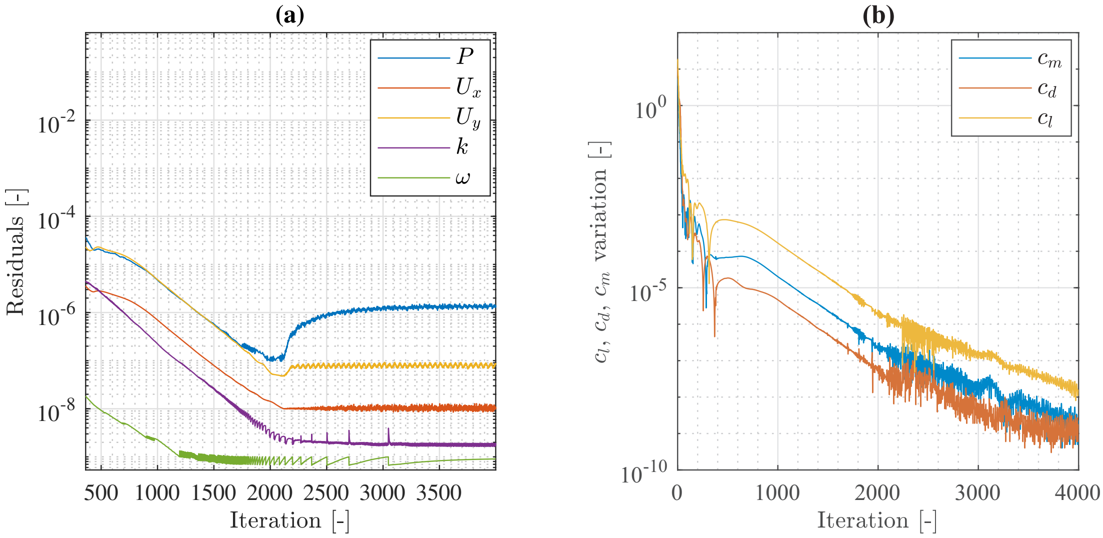

Fig. 2.10: At the left, residuals evolution during the iteration process. At the right, force coefficients variation evolution.

It is well known that residuals must not be the unique criteria to assess the simulation convergence. Because of this, a second convergence criterion is considered: the force coefficients variation (Figure 2.10b). It is defined as the maximum difference of the force coefficient c_x during the last 20 iterations.

Chapter 3

Results and discussion

This chapter discusses the CFD results of the different studied cases. The results are divided into two parts: firstly, a quasi-steady pitching motion case, where a very slow sweep will be imposed. Different turbulence model cases will be compared with experimental data available from Strangfeld et al.[11] and Timmer et al.[12]. An extensive discussion of the CFD and experimental data discrepancies will be conducted, examining the influence of some parameters such as the reduced frequency and the turbulence intensity in the quasi-steady results. Also, the accuracy of a 3D model compared to the 2D one will be studied.

Secondly, dynamic cases will be investigated, comparing CFD results with experimental ones for a low amplitude and fast frequency case. Then, a base case will be analysed, performing a physical interpretation of the obtained results through flow scenes and force coefficient plots. Lastly, the influence of reduced frequency, oscillation amplitude and turbulence intensity on dynamic stall behaviour will be examined.

3.1 Quasi-steady motion

In this section, results regarding the quasi-steady motion will be discussed. The quasi-steady motion term refers to cases where the reduced frequency is so low that results are very similar to the steady cases. Thus, unsteady lift effects, in this case, are negligible. Generally, a quasi-steady aerodynamics case can be considered if $k < 0.05$.

Experimental data for the quasi-steady motion using a NACA0018 aerofoil at $Re = 3 \cdot 10^5$ was measured by Strangfeld et al.[11] and Timmer et al.[12]. Both of them used a low turbulence intensity ($TI < 0.1\%$) and quantified the loads at the aerofoil's mid-span line (2D measurements). As it can be seen in Figure 3.1, results from both cases differ significantly.

In the Strangfeld et al. case, the maximum lift coefficient reaches $c_{lm}^{S} \approx 1.125$. On the Timmer et al. case it is significantly lower $c_{lm}^{T} \approx 1.05$. Besides, the abrupt stall point is quite larger in the Strangfeld et al. data ($\alpha_{as}^{S} \approx 20$ deg) than in the Timmer et al. ($\alpha_{as}^{T} \approx 17$ deg). Lastly, the Strangfeld et al. curve slope in the post-stall region is also slightly higher, leading to larger c_l values in this region.

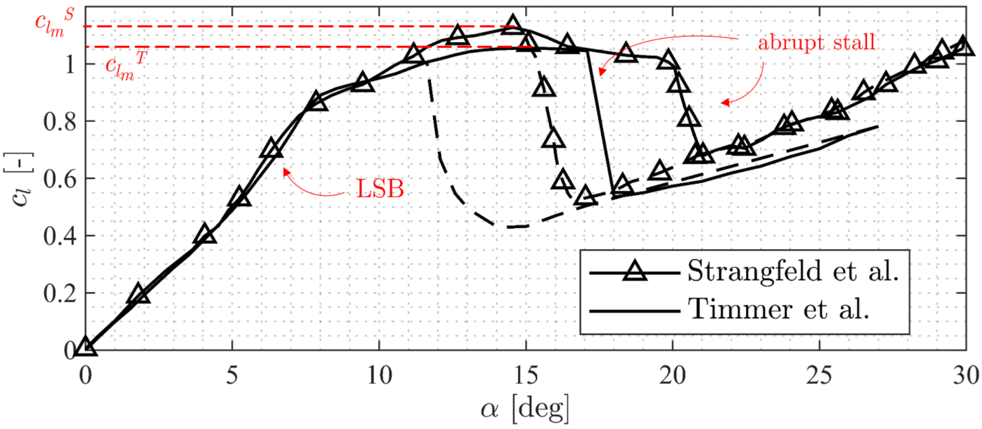

Fig. 3.1: Experimental data by Strangfeld et al.[11] and Timmer et al.[12] for the quasi-steady upstroke (solid line) and downstroke (dashed line) motions.

However, both sets of experiments agree on the pre-stall region slope, as well as the measurement of the laminar separation bubble (LSB) formed from $\alpha \approx 6$ deg, as well as in the hysteresis loop size $\Delta\alpha \approx 5$ deg.

Thus, despite two experimental setups with identical aerofoils and Reynolds number, similar turbulence intensity, amplitude and reduced frequency, results do not agree between them. Consequently, it demonstrates the complexity of correctly measuring and, therefore, modelling dynamic stall. For this project, the Strangfeld et al. data will be considered for model validation because of a complete description of the wind tunnel measurement parameters and better agreement with the obtained results.

Static cases

First of all, a static polar for the different turbulence models is calculated to assess the ability of static RANS simulations to reproduce the experimental data of the quasi-steady sweep. The results will be later compared to the obtained quasi-steady CFD results.

Results of static cases for $\alpha = [0, 26]$ deg for 2D cases using RANS k-ω SST, Langtry-Menter k-ω SST and Spalart-Allmaras and a 3D case using DES k-ω SST are shown in Figure 3.2. Cases are calculated using *simpleFoam* for low incidences (steady) and *pimpleFoam* for high ones (unsteady). First of all, it can be seen how the static cases can reproduce the proper slope for $\alpha < 5$ deg. From there, as the LSB appears, none of the cases except the transitional γ-Re_θ can predict the c_l correctly. The three other turbulence models assume a completely turbulent boundary layer, which is not the case of the NACA0018 at $Re = 3{\cdot}10^5$, where a transition between the laminar-turbulent boundary layer occurs.

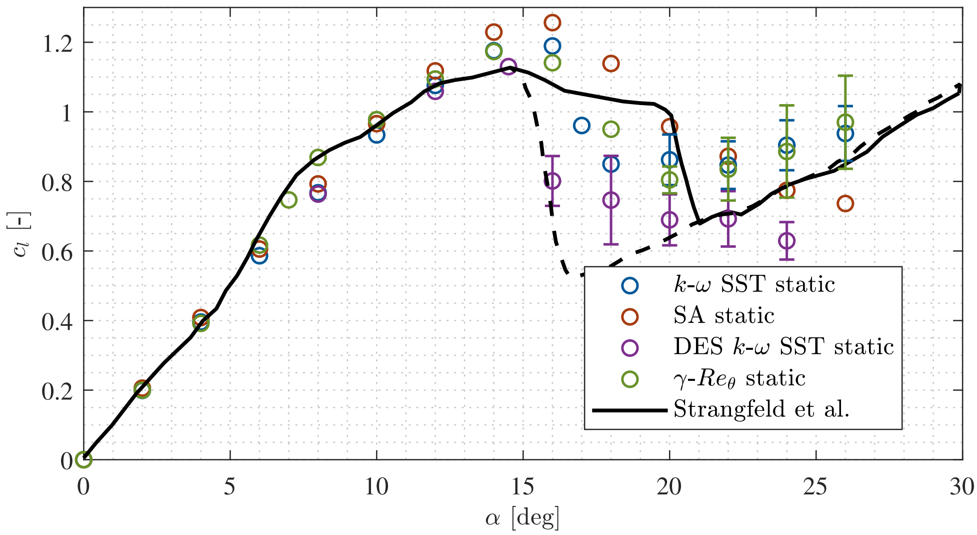

Fig. 3.2: Evolution of the c_l with the angle of attack α for static cases (circles) compared with the experimental quasi-steady upstroke (solid line) and downstroke (dashed line) results of Strangfeld et al.[11].

As shown in Figure 3.3, at minor incidences, a LSB is generated at the mid-chord. As the incidence increases, this LSB moves towards the leading edge, producing a growth of its virtual camber and increasing the c_l in this region. Besides, the rise of the adverse pressure gradient produces an earlier stall with respect to the turbulent boundary layer cases.

Furthermore, this LSB is noticeable by the negative suction peak in the pressure coefficient plot at the Langtry-Menter case, with a local increase on the c_p around $x/c \approx 0.06$. This explains the change of the slope and the increase in the c_l between $4 < \alpha < 10$ deg.

Moreover, all the 2D cases predict a slightly higher maximum lift coefficient c_{lm}, with a deviation of a 4.4% in the Langtry-Menter case ($c_{lm}|^{\gamma - Re_\theta} = 1.175$), 5.6% in the k-ω SST case ($c_{lm}|^{SST} = 1.19$) and 11% in the SA case ($c_{lm}|^{SA} = 1.26$). Besides, the 3D DES k-ω SST case shows an identical value with $c_{lm}|^{DES} = 1.13$.

In Figure 3.4, it can be seen that the suction peak at the RANS SST case is higher, explaining the increase in the maximum lift coefficient. In addition, the wake is larger also in this case, making the Δc_p slightly lower at the mid-chord ($0.2 < x/c < 0.6$). Besides, the closer the c_p to 0 at the TE ($x/c = 1$), the less intense the wake. Consequently, it can be stated that the wake is the smallest in the Langtry-Menter simulation.

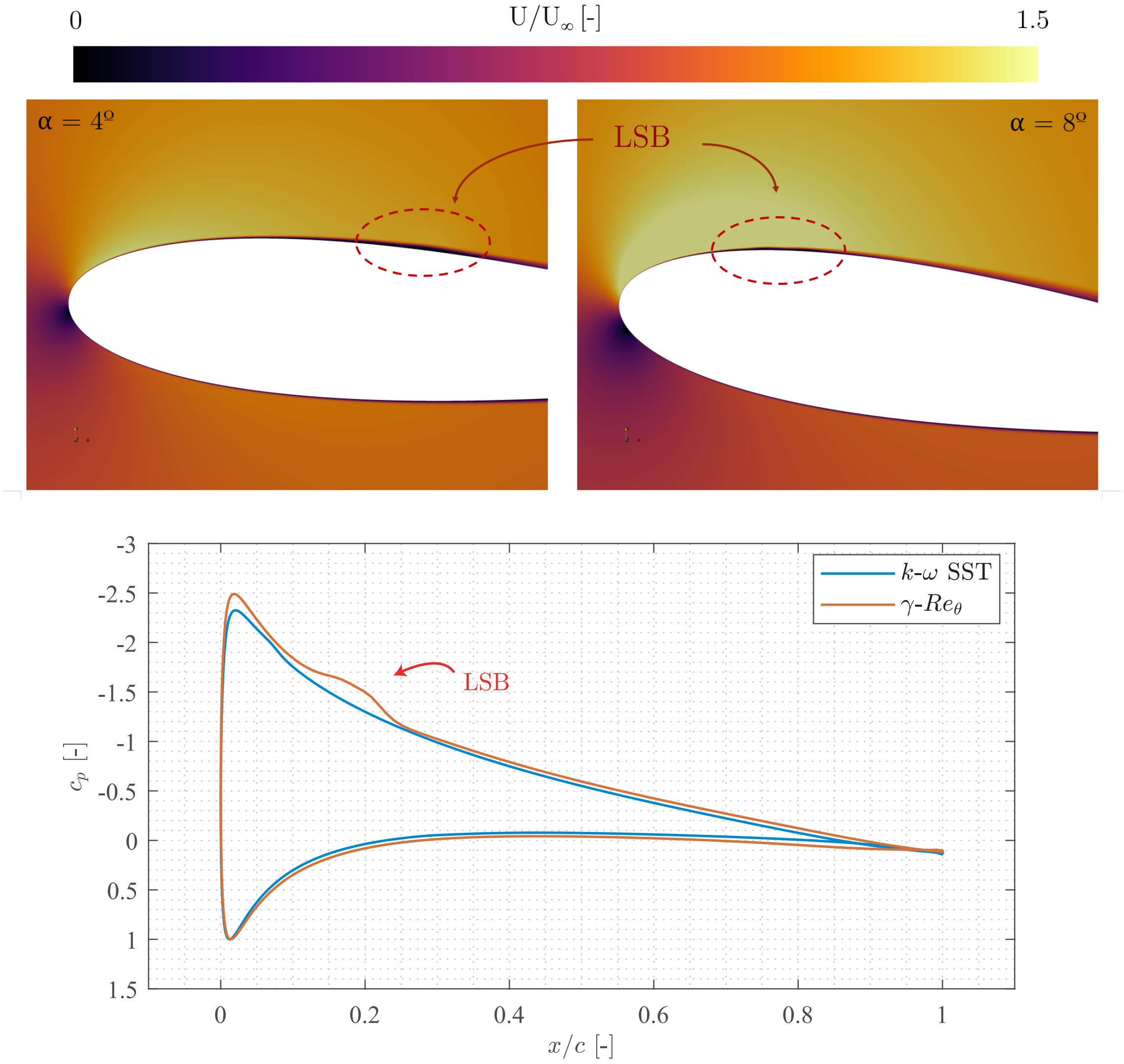

Fig. 3.3: At the top, dimensionless velocity U/U_∞ field showing the Laminar Separation Bubble (LSB) evolution at $\alpha = 4$ deg and $\alpha = 8$ deg. At the bottom, pressure coefficient c_p comparison between k-ω SST and Langtry-Menter k-ω SST at $\alpha = 8$ deg.

On the other hand, all three k-ω SST cases fail to reproduce the abrupt stall angle, most underestimated in the DES case. Furthermore, the SA case does not show any abrupt stall behaviour, being the worst model for this region. Besides, the DES case has a negative post-stall slope, while both the RANS k-ω SST and γ-Re_θ correctly predict a positive slope, although it is lower than in the experimental case.

The c_l prediction at the DES case is lower than in the other cases, as shown in the dimensionless velocity field at Figure 3.5, with a more aggressive stall behaviour.

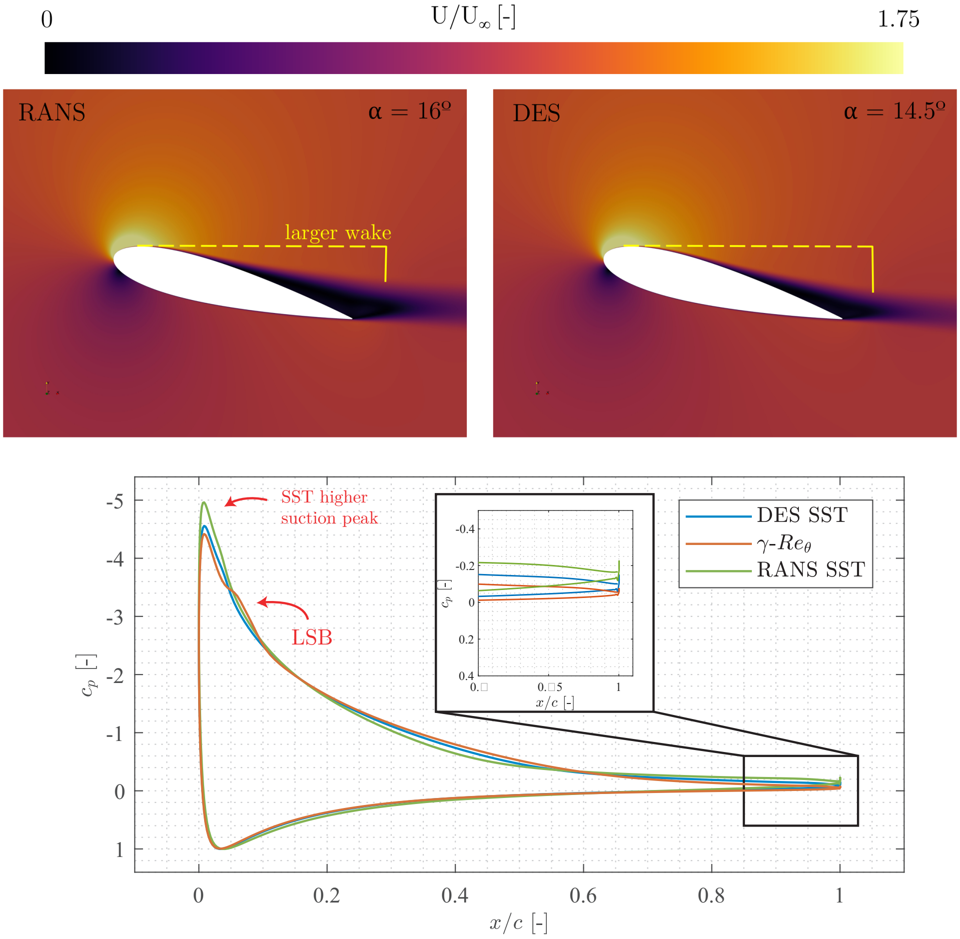

Fig. 3.4: At the top, dimensionless velocity U/U_∞ comparison between the RANS and the centre-line of the DES k-ω SST cases at $c_l = c_{lm}$. At the bottom, pressure coefficient c_p for the three k-ω SST cases at $c_l = c_{lm}$.

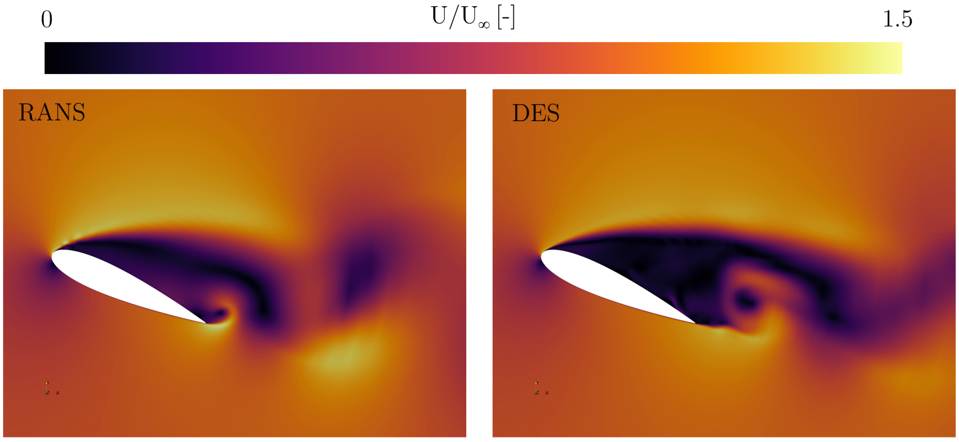

Fig. 3.5: Comparison of dimensionless velocity U/U_∞ field between the RANS and DES k-ω SST cases at $\alpha = 24$ deg.

Discrepancies in the DES case can be mainly caused by the unsteady lift effects on the experimental data due to the aerofoil's motion, which are known to delay stall. Besides, the lack of precision of RANS models to calculate highly turbulent and separated flows can be the principal cause of the differences in these cases.

In conclusion, none of the four static cases successfully reproduced the experimental results. However, the static k-ω SST cases show a good agreement on the maximum lift coefficient (especially the DES case) and the appearance of an abrupt stall. Nevertheless, the prohibitively expensive computational cost of 3D DES cases makes it essential to study the usefulness of simulating high fidelity approaches such as DES in unsteady cases. Due to this, the DES approach will be discarded as, although it is true that it shows a better agreement with the experimental data, the cost is considered excessively large with the available computational resources for this MSc thesis.

Quasi-steady cases

Once the static results have been analysed, the results of the quasi-steady CFD simulations will be shown and compared with the experimental data. URANS cases with k-ω SST, Spalart-Allmaras and Langtry-Menter k-ω SST are considered for the quasi-steady loop. As stated before, DES cases are discarded due to the high computational cost.

In Table 3.1 are presented the motion parameters and conditions of the four cases. They start from $\alpha_0 = 0$ deg, but the amplitude for the CFD cases does not reach 30 degrees to save computational cost. The solution in the post-stall region is the heaviest to calculate, and the results follow the same tendency in the whole region.

Case	α_0 [deg]	α_1 [deg]	f [Hz]	k [-]	TI [%]
Strangfeld et al.	0	30	0.001	$8.5 \cdot 10^{-5}$	< 0.1
k-ω SST (1)	0	28	0.01	$6.3 \cdot 10^{-4}$	0.05
Spalart-Allmaras (2)	0	28	0.01	$6.3 \cdot 10^{-4}$	0.05
Langtry-Menter k-ω SST (3)	0	26	0.01	$6.3 \cdot 10^{-4}$	0.5

Table 3.1: Motion parameters of the quasi-steady cases.

Moreover, the experimental frequency is significantly lower than in the computed cases. The selected frequency of $f = 0.01$ Hz is expected to be low enough to keep the quasi-steady assumption accurate and save simulation time. Notice that simulating a ten times lower frequency increases at least ten times the simulation cost, as the motion's period is inversely proportional to the frequency. However, it must be considered when comparing results that the frequency is not the same.

Finally, it is essential to remark that case 3 has a higher turbulence intensity due to the numerical instability faced when setting it lower than 0.5%. Thus, it was not possible to get results for the Langtry-Menter k-ω SST at lower TI. As shown in Figure 3.6a, a lower value of turbulence intensity increases the hysteresis loop and the sudden loss of lift at the abrupt stall point. However, the influence of TI becomes smaller at lower values.

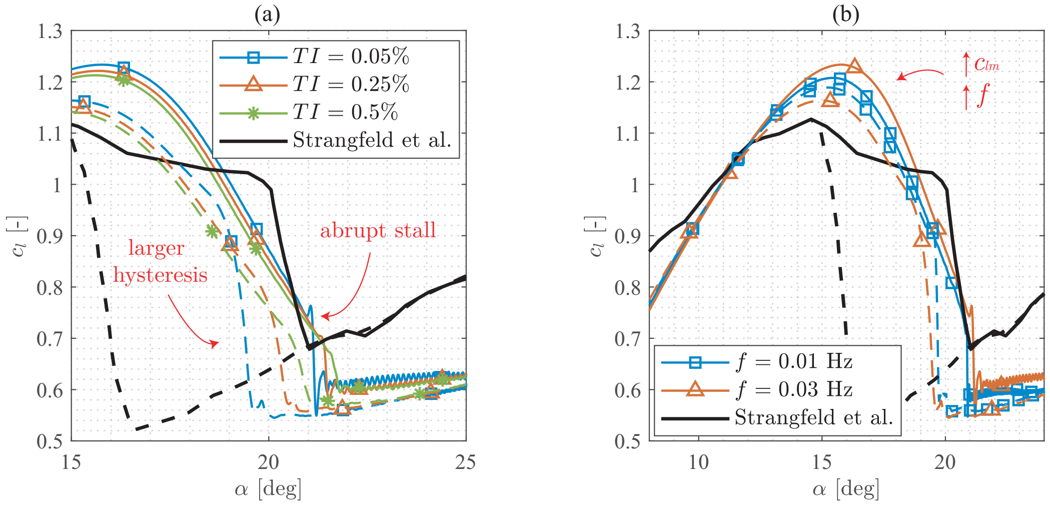

Fig. 3.6: At the left, effect of turbulence intensity on the quasi-steady solution. On the right, influence of the motion's frequency in the quasi-steady solution. Upstroke in solid line, downstroke in dashed line.

Results for the described cases are shown in Figure 3.7, with close-ups of the key regions such as the stall angle and the deep stall region. In the linear phase, it can be seen how the non-transitional models cannot predict the LSB. On the other hand, the Langtry-Menter results greatly agree with the experimental data on this linear region.

Regarding the stall point, in Figure 3.7b it is clear that all the URANS cases overestimate the maximum c_l, especially the Spalart-Allaras turbulence model ($\Delta c_{l_m}|^2 = 0.1$). In the SST cases, this difference is lower, $\Delta c_{l_m}|^1 = 0.08$ and $\Delta c_{l_m}|^3 = 0.03$. Thus, these two cases capture the maximum lift coefficient with a deviation of a 7.1% and 2.6%, respectively.

Besides, part of this could be explained by the higher reduced frequency of the simulations respect to the experimental case. In Figure 3.6b it is demonstrated the influence of frequency in the c_l curve: the maximum c_l decreases with lower frequency. Consequently, a ten times higher frequency could explain part of the discrepancies.

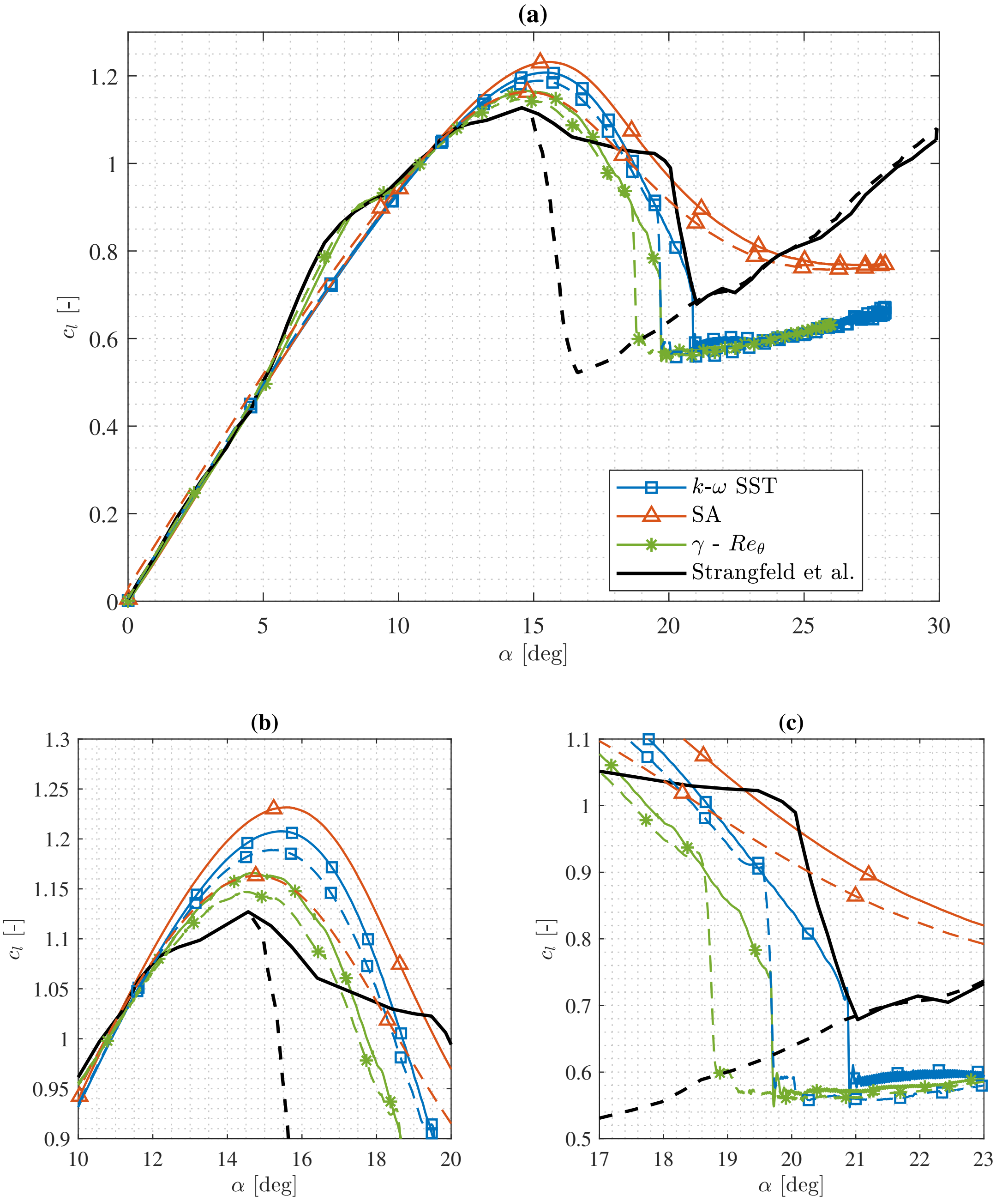

Fig. 3.7: At (a), evolution of the c_l with the angle of attack α during the quasi-steady upstroke (solid line) and downstroke (dashed line) motions for different turbulence models. At (b), close-up view of the maximum c_l zone. At (c), close-up view of the abrupt stall zone.

Although the URANS solution shows good agreement with the experimental data in this region, all the cases fail to predict the air loads in the abrupt and post abrupt-stall region (Figure 3.7c). Firstly, as in the static case, the Spalart-Allmaras turbulence model does not predict an abrupt stall. Furthermore, the SST cases predict a lighter stall behaviour with respect to the experimental data. Finally, the transitional Langtry-Menter turbulence model is closer in the estimation of the abrupt-stall angle, $\Delta\alpha_{as}|^3 = 0.25$ deg, than the base k-ω SST case, $\Delta\alpha_{as}|^1 = 1$ deg.

From Figure 3.8, it can be concluded that the SST and SA cases show a similar dimensionless velocity field before the abrupt stall angle, with a slightly higher suction peak on the SA case, which leads to a more considerable c_l value. After the abrupt stall, the SST case shows a more aggressive and twisted wake, while the SA suffers an increase in the wake width and a reduction of the suction peak.

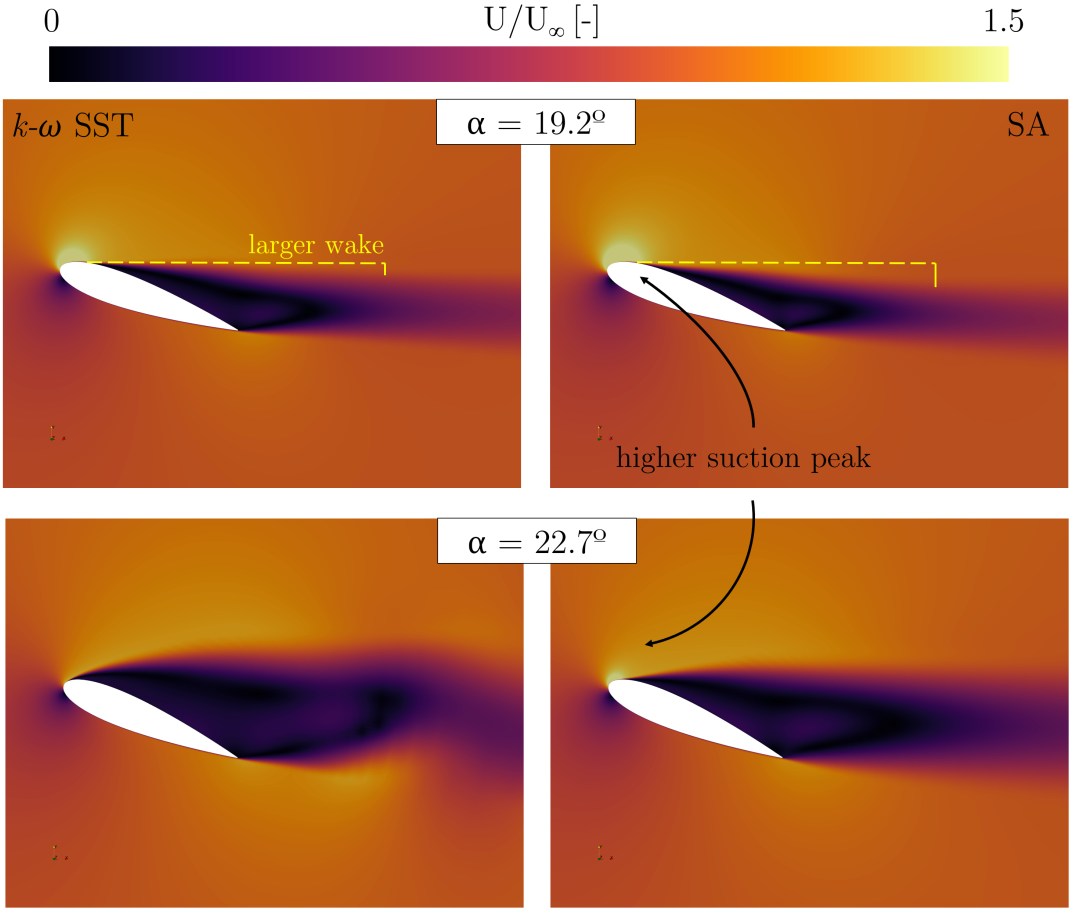

Fig. 3.8: Comparison of the dimensionless velocity U/U_∞ between the k-ω SST and the SA cases before and after the abrupt stall angle, $\alpha = 19.2$ deg and $\alpha = 22.7$ deg, respectively.

As shown in Figure 3.9, the SST turbulence model predicts an interaction of the clockwise and anticlockwise turbulent structures and a mixing of them downstream of the aerofoil due to a lower pressure value on the upper wake zone. Alternatively, in the SA solution, the structures are simply a prolongation of the leading and trailing edges. This lack of interaction could be caused by the simplicity of the Spalart-Allmaras model, which only uses one equation to predict the turbulent behaviour.

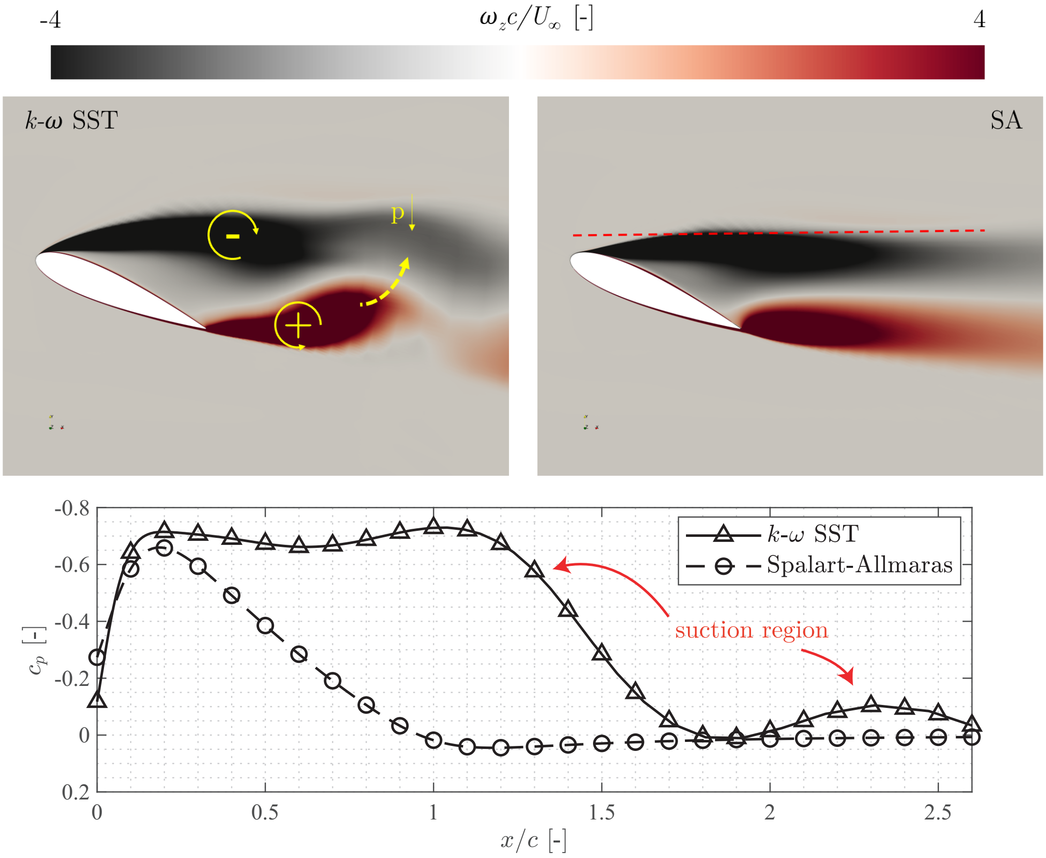

Fig. 3.9: At the top, comparison of the dimensionless z-axis vorticity $\omega_z c/U_\infty$ between the k-ω SST and the SA cases after the abrupt stall angle, $\alpha = 22.7$ deg. At the bottom, pressure coefficient c_p downstream of the leading edge (red dashed line) for both cases.

On the other hand, URANS simulations cannot reproduce the post-stall region. The slope of both SST cases is significantly lower than the experimental one. Moreover, the hysteresis loop in the experimental case does not appear in the CFD simulations. These discrepancies are common in almost all the 2D URANS simulations of low sweep pitching aerofoils found in the literature. Strangfeld et al.[11] concluded that it is essential to conduct three-dimensional computations when compared to wind tunnel experiments, especially at higher angles of attack, as the side wall-wing interaction has a significant impact on this situation. McCroskey et al. also found a powerful influence of it on the wind tunnel measurements [15].

Furthermore, it is known that URANS struggles when predicting flows with highly turbulent flow, especially in two-dimensional cases, due to the three-dimensional behaviour that characterises turbulence. As explained in Section 1.3, some authors have pointed out that URANS tends to overestimate eddy viscosity at the wake of the aerofoil, blurring wake structures and thus not being reliable in high turbulence conditions.

To solve this, some authors propose the modification of the turbulence model coefficients to adapt it to the desired flow behaviour. In Figure 3.10 it is demonstrated the effect of changing the k-ω SST model coefficient α_1 which has significant relevance to the eddy viscosity estimation. It is important to remark that the modification of the turbulence model coefficients leads to a breakage of the model calibration and, consequently, a worse estimation of the wall shear stress. Besides, numerical stability issues have been found in this project when changing α_1 drastically. Thus, $\alpha_1 = 0.307$ is the minimum value that has been possible to achieve without compromising the solution convergence.

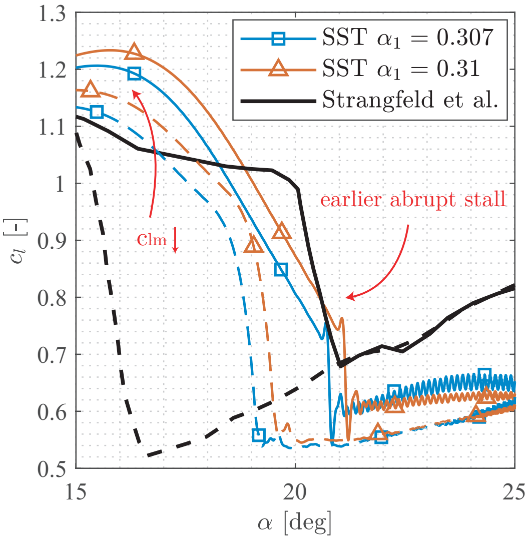

Fig. 3.10: Influence of α_1 in the c_l vs α curve in the quasi-steady case.

A reduction of the maximum lift coefficient c_{lm} and the abrupt stall angle α_{as} is achieved. However, the hysteresis loop size remains quite similar, and the c_l decay at this point is still significantly lower than in the experimental data.

Finally, comparing the obtained two-dimensional solution with a three-dimensional case is convenient, as this simplification could induce a significant error. Thus, a 2D and 3D case comparison is shown at Figure 3.11. The frequency is higher than in the previous cases, $f = 0.05$ Hz, and the amplitude is lower, $\alpha_1 = 24$ deg, to cope with the high computational cost of the three-dimensional approach.

First of all, both cases show an identical slope in the pre-stall phase, as well as the same c_{lm}. Thus, the induced tip vortex generated due to the pressure and suction side pressure difference has a minor influence on this motion. As stated before, the main parameter influencing the deviation in the c_{lm} estimation is the relatively high frequency used to save computational time.

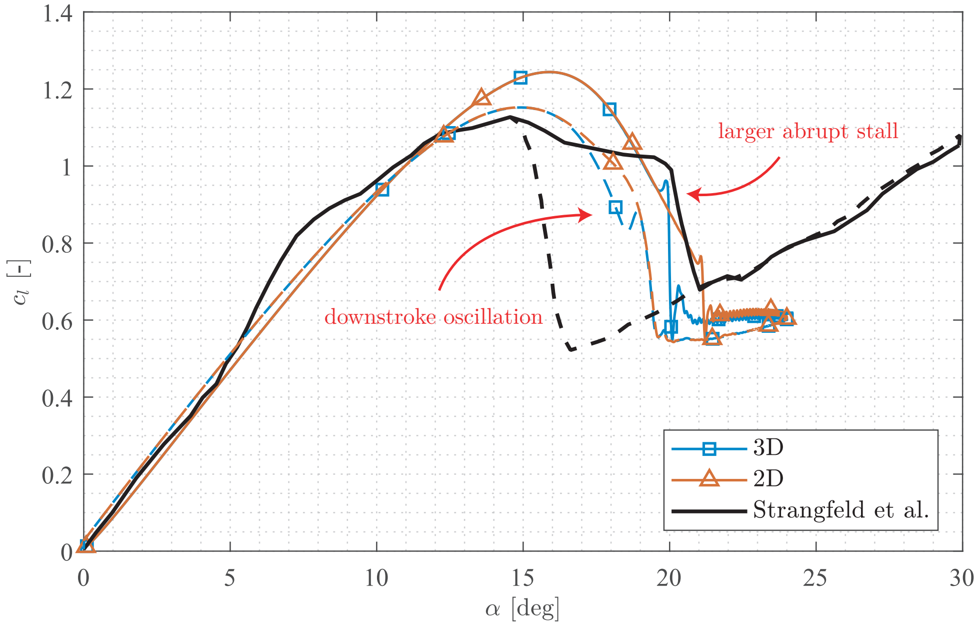

Fig. 3.11: Comparison between a 2D and 3D case during the quasi-steady upstroke (solid line) and downstroke (dashed line) motions.

On the other hand, there is a change in the abrupt stall zone: the sudden loss of lift in the three-dimensional case is predicted to be larger than in the two-dimensional one. The 3D case shows a great agreement with the experimental data in terms of the abrupt start beginning, $\alpha_{as}|^{3D} \approx 20$ deg and lift coefficient decay, $\Delta c_{l_{as}}|^{3D} = 0.35$. Furthermore, there is a slight difference in the downstroke motion, with a light decay at the three-dimensional case at $\alpha \approx 19$ deg. These differences are visible in the flow-field, as demonstrated in Figure 3.12.

Consequently, it can be stated that the major difference between the 3D and 2D approaches for the quasi-steady movement is the better prediction of the abrupt stall behaviour (Figure 3.13). The two-dimensional approach has been demonstrated to diffuse the stall behaviour, estimating a smoother abrupt stall.

However, the deficiencies in the post-stall region and the downstroke motion prediction are still present in the three-dimensional case. Thus, it can be concluded that the URANS approach, both with and without two-dimensional assumption, cannot correctly estimate the flow behaviour at the highly turbulent regimes for the quasi-steady motion.

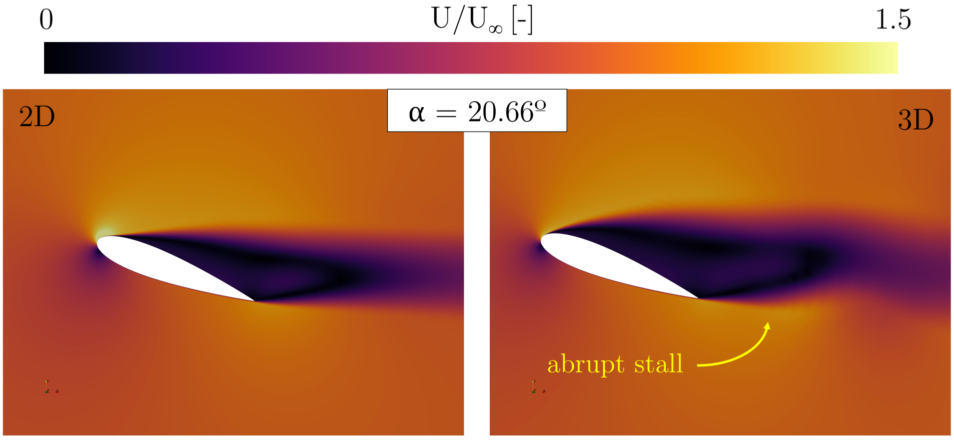

Fig. 3.12: Comparison of the dimensionless velocity U/U_∞ between the two-dimensional case and the three-dimensional (mid-span) one after the 3D abrupt stall, $\alpha = 20.66$ deg.

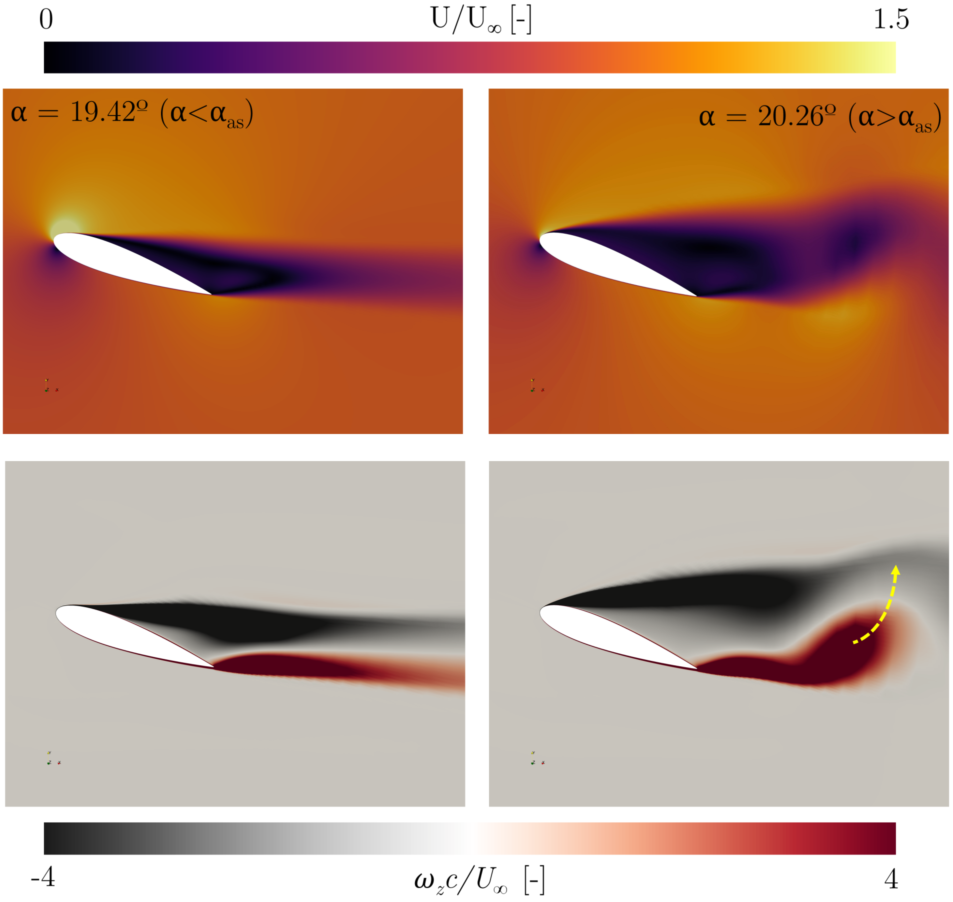

Fig. 3.13: At the top, dimensionless velocity U/U_∞ before and after the abrupt stall for the three-dimensional case, $\alpha = 19.42$ deg and $\alpha = 20.26$ deg, respectively. At the bottom, the same but for the dimensionless vorticity field $\omega_z c/U_\infty$.

Another validation with experimental data for the quasi-steady case is possible. In Figure 3.14, a comparison between the pressure coefficient for $\alpha = 14.5$ deg is shown for the most relevant cases analysed in this section. The three-dimensional case is not included as its result is similar to the two-dimensional one for this incidence (Figure 3.11).

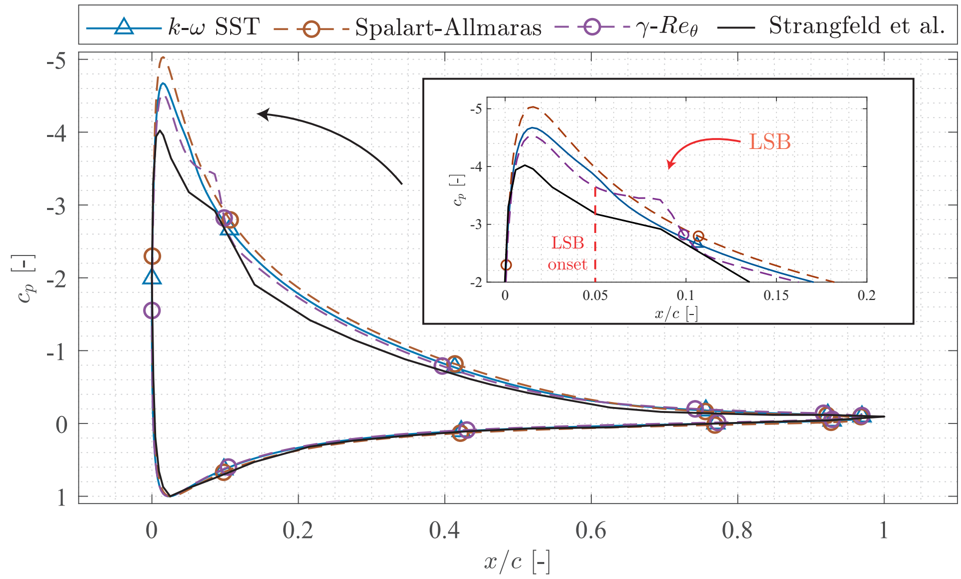

Fig. 3.14: Comparison of the pressure coefficient c_p between Strangfeld et al. experimental data [11] and the URANS k-ω SST, Spalart-Allmaras and Langtry-Menter cases at $\alpha = 14.5$ deg with close-up to the suction peak and LSB zone.

As predictable, the suction peak in all the three cases is overestimated, leading to a higher c_{lm}. As explained before, the Langtry-Menter is the one which better reproduces the experimental data in this zone, with a slightly lower $c_{p_{\min}}$ (absolute value), as well as the prediction of the laminar separation bubble at $x/c \approx 0.05$. However, the suction estimation is higher along the whole aerofoil's surface. Although discrepancies exist between the experimental data and the obtained results, they could be mainly caused due to the higher frequency of the CFD cases. Thus, the k-ω SST results are good in this zone, with deviations lower than 10%.

In Figure 3.15 it can be seen a comparison between the relative computational cost of the tested turbulence models in this section. It is important to remark that both the DES k-ω SST and 3D k-ω SST cases were solved using 32 CPUs, while the rest were done using 16 CPUs. As explained before, the SA is the cheapest one, but it is the worst at predicting the air loads. The Langtry-Menter turbulence model has 2.4 times more computational cost than the base k-ω SST, and the 3D DES and RANS k-ω SST have a significantly higher cost.

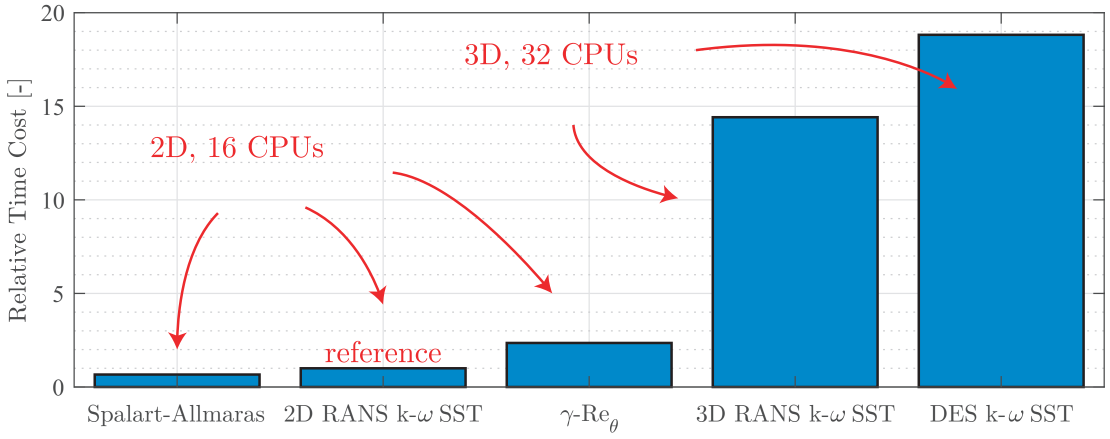

Fig. 3.15: Relative time cost for each tested approach for the quasi-steady motion in an unsteady simulation of 1 second.

To give a reference, the shown cost is for an unsteady case solved using pimpleFoam. The total simulation time was 1 second. The absolute computational cost for the base k-ω SST was 32 minutes. A quasi-steady simulation of $f = 0.01$ Hz, which has a simulation time of 50 seconds, needs approximately 27 hours to achieve a solution. Thus, the computational cost associated with the quasi-steady cases is significantly high, especially considering the project's scope.

The 3D cases are discarded because of the prohibitive computational cost. The SA model is not used because of the lack of accuracy. Besides, the Langtry-Menter turbulence model doubles the computational cost of the base SST one, and numerical instability has been found while using it. Consequently, the base 2D k-ω SST case will be used to study dynamic stall for the rest of the project.

3.2 Fast sweeps

Once the quasi-steady sweep case has been studied, fast sweep motions will be calculated in this section to continue with the model validation considering a different type of motion. Experimental data of a small amplitude, $\alpha_1 = 2$ deg, and low-high frequencies, $k = 0.08$ and $k = 0.263$ motion starting at $\alpha_0 = 2$ deg is compared with the obtained results for two and three-dimensional cases in Figure 3.16.

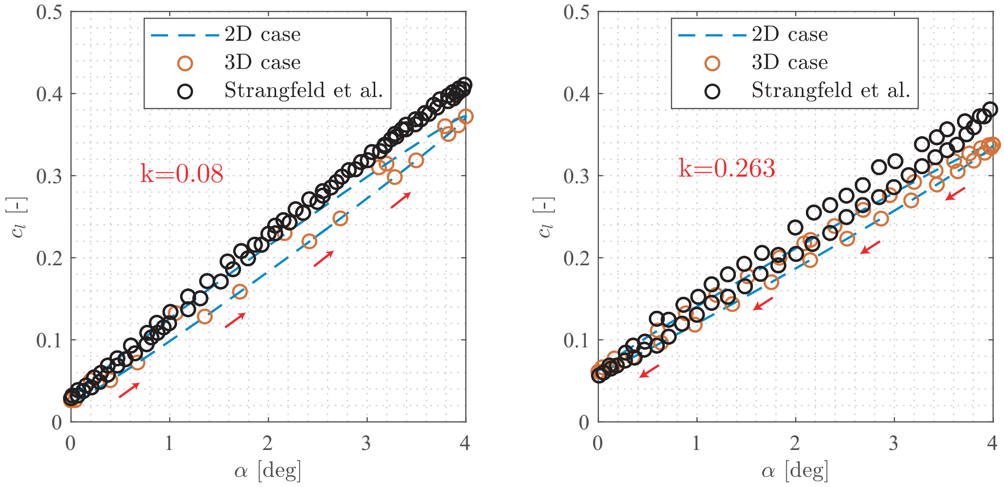

Fig. 3.16: Comparison of lift coefficient c_l results for fast sweep motions ($\alpha_0 = 2$ deg, $\alpha_1 = 2$ deg, $k = 0.08$ and $k = 0.263$) between experimental data by Strangfeld et al.[11], 2D and 3D cases.

First of all, in this case, no difference is found between the 2D and 3D solutions, as the movement implies incidences far from the stall, where the main differences were found in the quasi-steady case. In the case of low frequency, the slope of the CFD results is close to the quasi-steady case, indicating a low influence of the unsteady lift effects. However, the slope is reduced, especially in the medium frequency case. Furthermore, CFD results properly predict the rotational sense of the curve, with an anticlockwise sense for $k = 0.08$ and clockwise for $k = 0.263$.

On the other hand, experimental results at low incidence are correctly estimated, obtaining identical results in both cases for $\alpha = 0$ deg. Nevertheless, results gradually differ once the incidence rises, with deviation up to 10% at $\alpha = 4$ deg. Once more, results deficiencies can be caused due to the URANS approach not estimating the unsteady turbulence structures correctly. However, the deviation is considered low enough to analyse the dynamic stall phenomenon.

3.3 Dynamic stall analysis

Once the URANS simulations have been proven to be accurate enough for quasi-steady and fast sweeps, a physical analysis of the dynamic stall is carried out using CFD results. For this, a case of deep dynamic stall is considered, with a mean angle $\alpha_0 = 14$ deg, amplitude $\alpha_1 = 14$ deg ($\alpha_m = 28$ deg) and reduced frequency $k = 0.063$ ($f = 1$ Hz). The c_l results are shown in Figure 3.17, with the indicated key points corresponding to the scenes displayed at Figure 3.18.

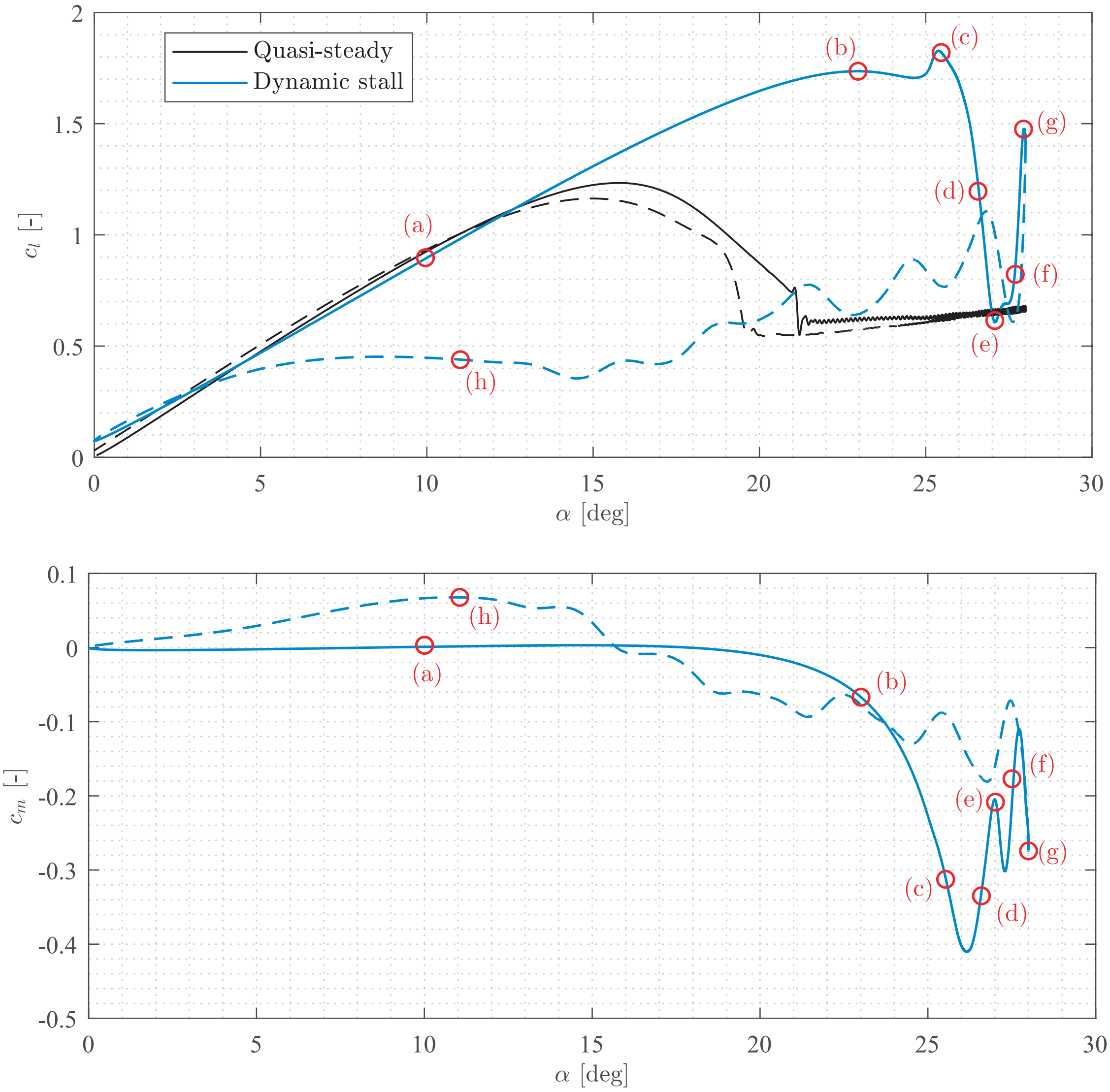

Fig. 3.17: At the top, lift coefficient c_l results of a deep dynamic stall case ($\alpha_0 = 14$ deg, $\alpha_1 = 14$ deg, $k = 0.063$) with key points indicated by letters. At the bottom, moment coefficient c_m for the same motion. Solid line for the upstroke, dashed line for the downstroke.

At the beginning of the motion, no significant differences appear with respect to the quasi-steady case (a). The slope of the dynamic case is slightly lower since the frequency is higher. A high suction peak appears on the leading edge. Due to the large adverse pressure gradient at the suction side, the flow detaches at most of the chord. However, as the flow is not entirely unattached, this state can be classified as the *attached flow* stage.

As the incidence raises (b), the *stall development* stage starts: flow at the leading edge is entirely unattached, and the suction peak disappears. However, the Primary Dynamic Stall Vortex (PDSV) starts to develop, causing a decrease in the pressure at the aerofoil's mid-chord. Thus, the c_l increases while the PDSV grows until the maximum lift coefficient is reached (c).

Simultaneously, the counterclockwise Induced Vortices (IVs) are generated due to the interaction between the unattached flow and the PDSV. During this process, a significant part of the lift force is generated at the rear part of the aerofoil. Thus, an anticlockwise pitching moment (negative) appears at the aerofoil and rises until a massive value when the PDSV is fully developed.

The IVs are pushed towards the leading edge, causing the PDSV detachment and, consequently, a sudden decrease in the c_l and c_m (absolute value) due to the plateau at the c_p in most of the aerofoil's chord (d), leading to the *stall onset*. However, the Trailing Edge Vortex (TEV) enlarges and causes a temporary growth on the suction at the trailing edge until it is pushed downstream, causing a significant c_l and c_m drop (e).

The *stalled stage* (f) is characterised by unattached flow at most of the aerofoil's suction side. As incidence reaches its maximum value, a Secondary Dynamic Stall Vortex (SDSV) is generated, starting the explained process again (g). However, as can be seen in the c_p, c_l and c_m at this point, this vortex strength is lower than before.

The vortex generation and shedding process is repeated during the whole downstroke causing rapid rises and decreases on the c_l and c_m until the *flow reattachment* stage is reached (h).

As demonstrated, the URANS k-ω SST simulations can reproduce the most important physics of the dynamic stall at the pitching NACA0018 aerofoil. All the phases of the phenomenon occur in the simulations, and the theoretical characteristics described at section 1.4 have been identified in the CFD results. Thus, the CFD simulations can qualitatively describe the PDSV, IV and TEV formation and shedding, as well as estimate their effect on the air loads.

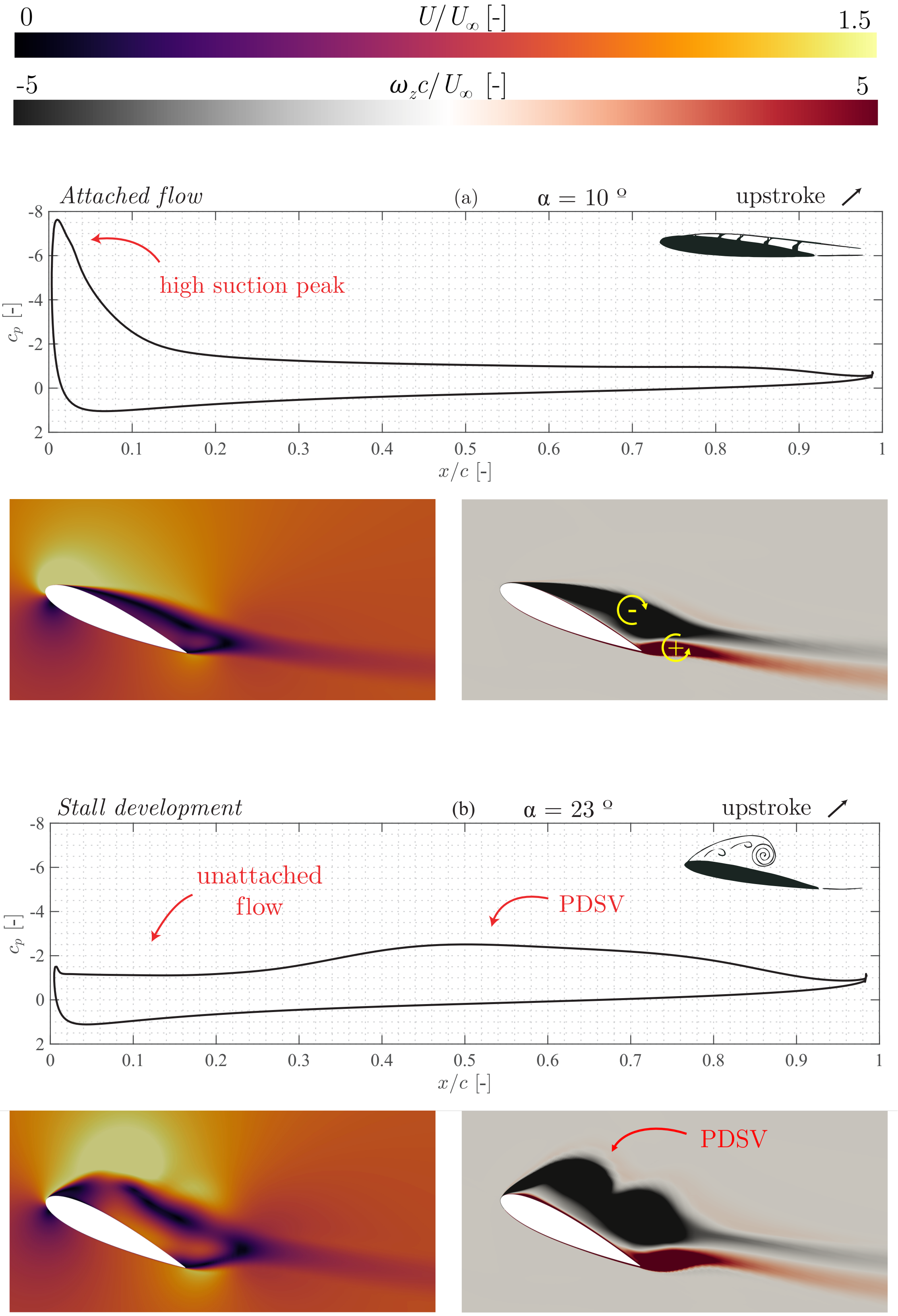
0
U/U_∞ [-]
1.5
-5
$\omega_z c/U_\infty$ [-]
5
Attached flow
(a)
$\alpha = 10$ º
upstroke
high suction peak
c_p [-]
x/c [-]
-8
-6
-4
-2
0
2
0
0.1
0.2
0.3
0.4
0.5
0.6
0.7
0.8
0.9
1
-
+
Stall development
(b)
$\alpha = 23$ º
upstroke
unattached flow
PDSV
c_p [-]
x/c [-]
PDSV

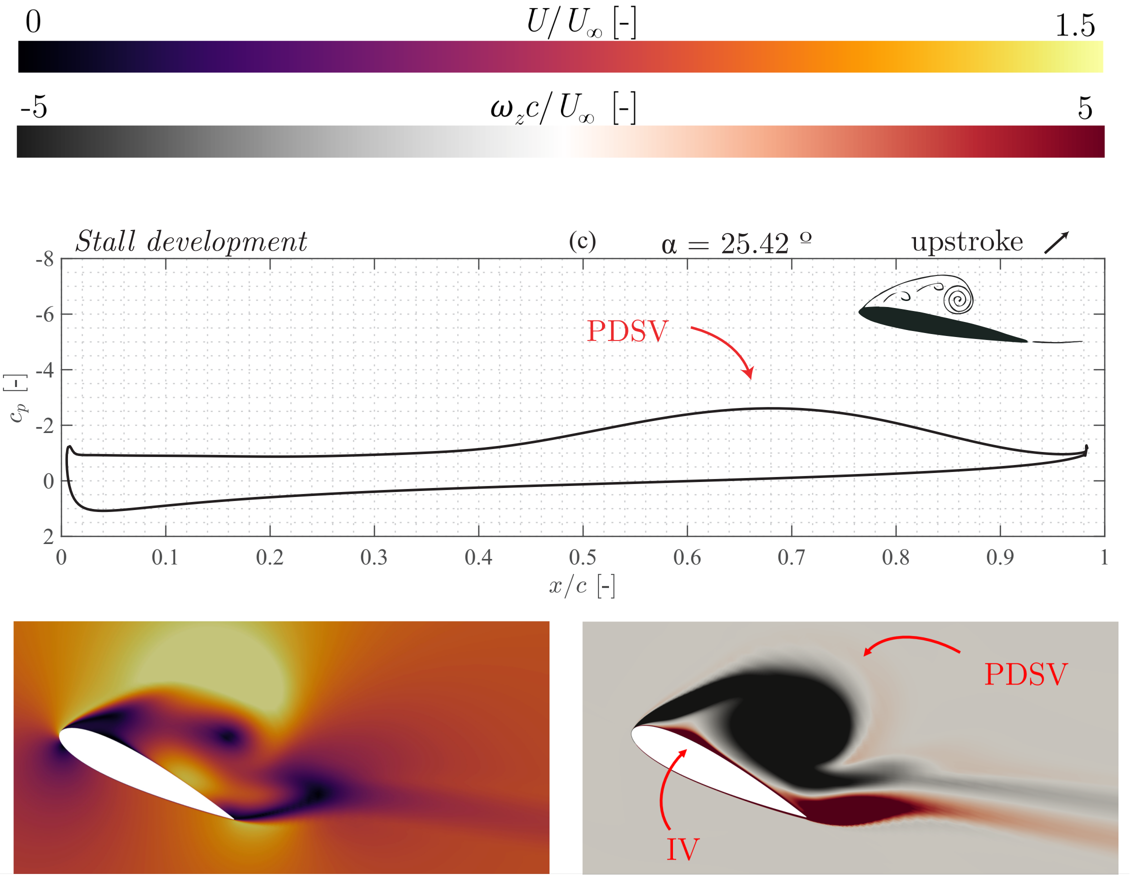
0
U/U_∞ [-]
1.5
-5
$\omega_z c/U_\infty$ [-]
5
Stall development
(c)
α = 25.42 º
upstroke
PDSV
-8
-6
-4
-2
0
2
c_p [-]
0
0.1
0.2
0.3
0.4
0.5
0.6
0.7
0.8
0.9
1
x/c [-]
PDSV
IV

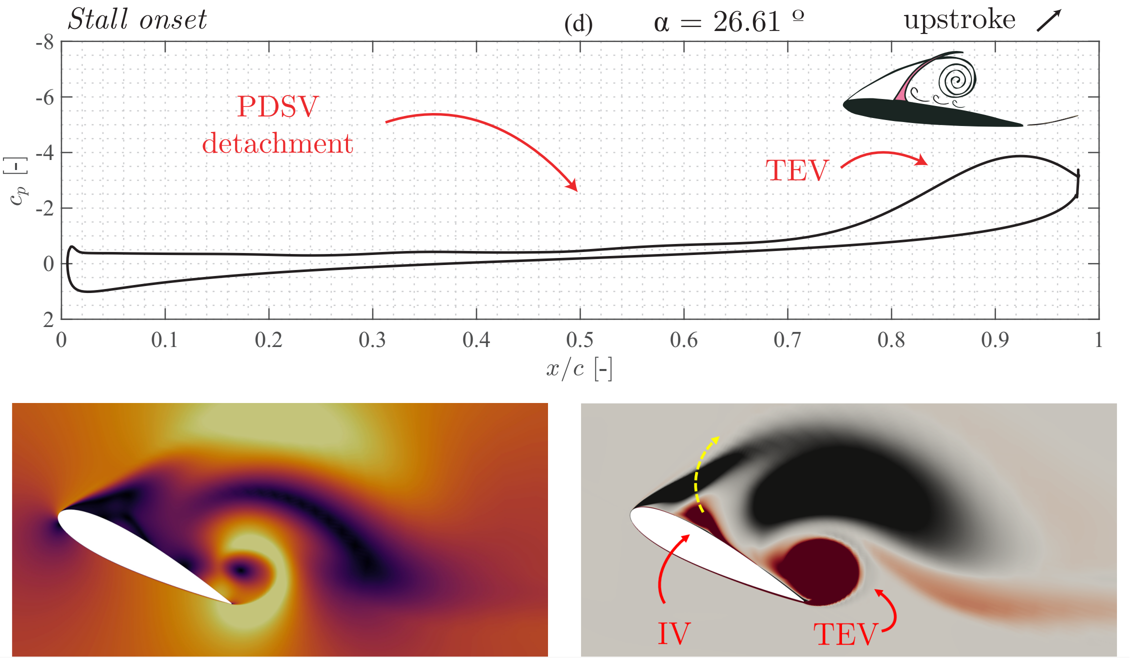
Stall onset
(d)
α = 26.61 º
upstroke
PDSV
detachment
TEV
-8
-6
-4
-2
0
2
c_p [-]
0
0.1
0.2
0.3
0.4
0.5
0.6
0.7
0.8
0.9
1
x/c [-]
IV
TEV

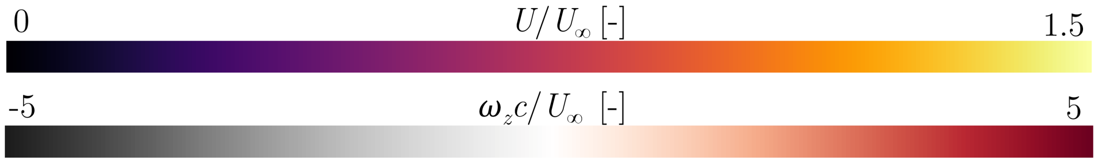
0
U/U_∞ [-]
1.5
-5
$\omega_z c/U_\infty$ [-]
5

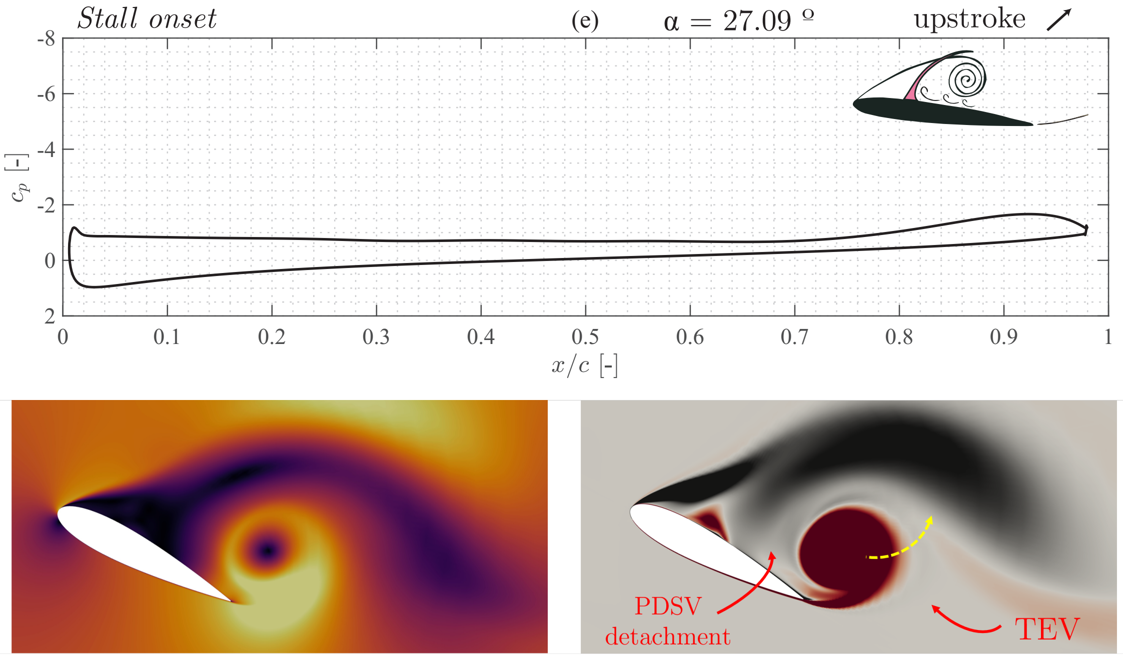
Stall onset
(e)
α = 27.09 º
upstroke
c_p [-]
-8
-6
-4
-2
0
2
0
0.1
0.2
0.3
0.4
0.5
0.6
0.7
0.8
0.9
1
x/c [-]
PDSV
detachment
TEV

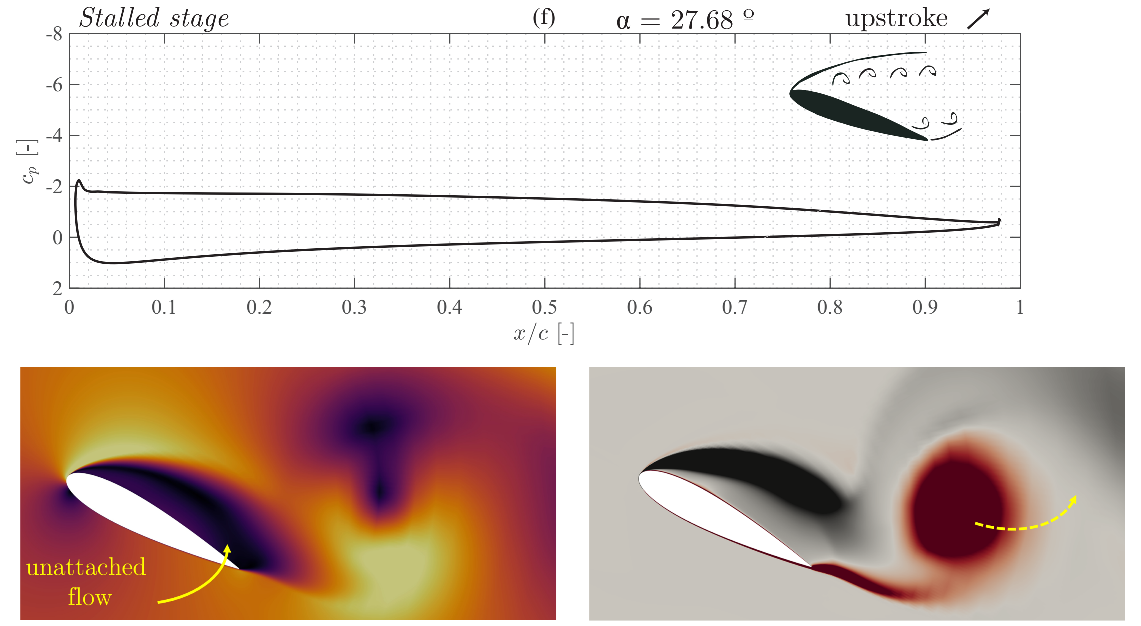
Stalled stage
(f)
α = 27.68 º
upstroke
c_p [-]
-8
-6
-4
-2
0
2
0
0.1
0.2
0.3
0.4
0.5
0.6
0.7
0.8
0.9
1
x/c [-]
unattached
flow

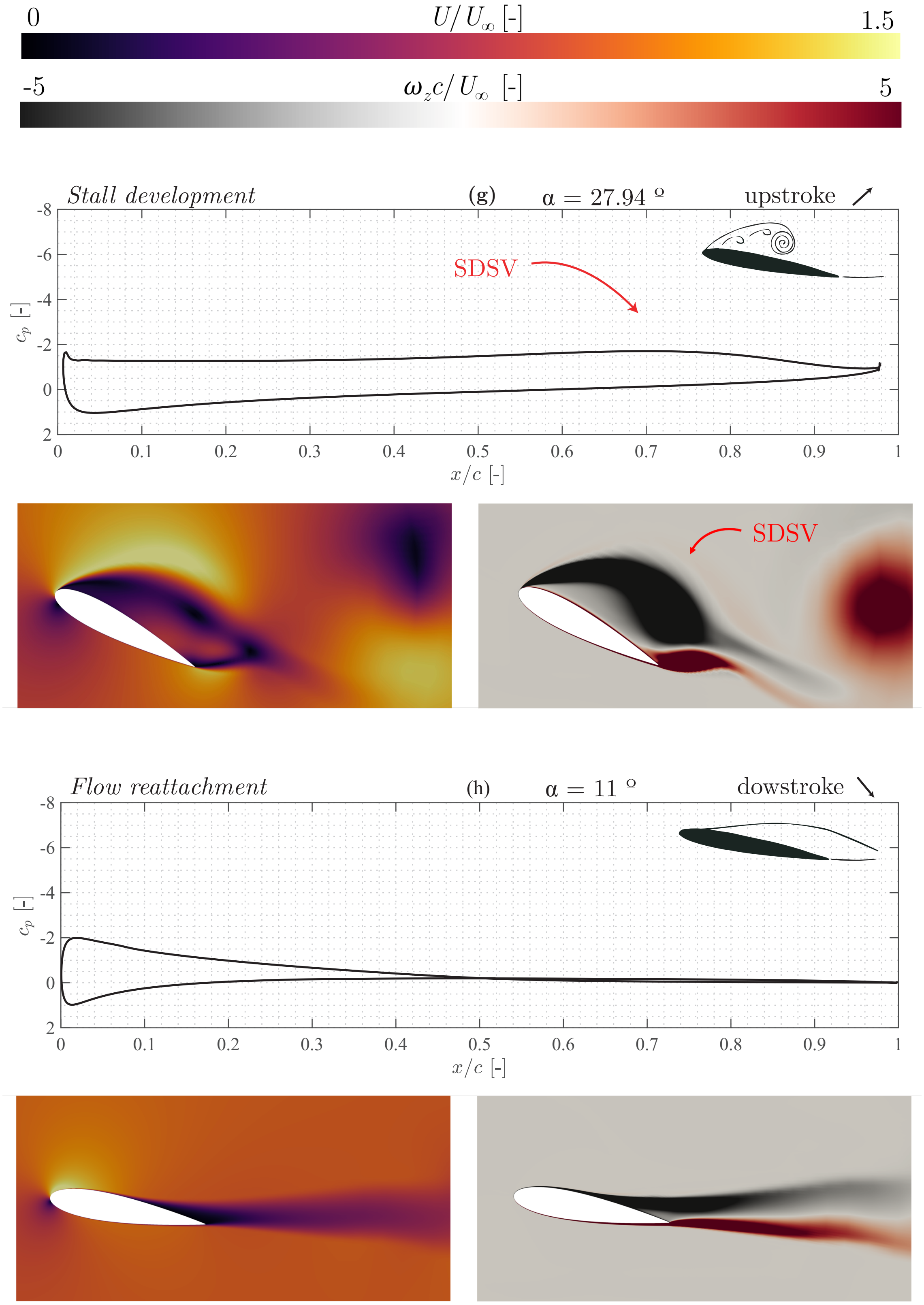

Fig. 3.18: Pressure coefficient c_p plot, dimensionless velocity U/U_∞ and vorticity $\omega_z c/U_\infty$ for different incidences through the sweep motion ($\alpha_0 = 14$ deg, $\alpha_1 = 14$ deg, $k = 0.062$).

3.4 Dynamic stall influences

This section will analyse the impact of several parameters in the dynamic stall phenomenon: reduced frequency, k, motion amplitude, α_1 and inlet turbulence intensity, TI. For this, two-dimensional URANS simulations with the k-ω SST turbulence model will be solved. Moreover, some three-dimensional cases will also be run to assess if the dimensional choice is relevant in dynamic stall cases.

Reduced frequency

First of all, the reduced frequency effect will be studied. For this, different cases are prepared: (1) slow ($f = 0.4$ Hz; $k = 0.025$), (2) medium ($f = 1$ Hz; $k = 0.063$) and (3) high ($f = 1.6$ Hz; $k = 0.1$) frequency cases will be solved. The other motion parameters chosen are a mean angle of $\alpha_0 = 14$ deg and amplitude of $\alpha_1 = 10$ deg. Results are shown at Figure 3.19.

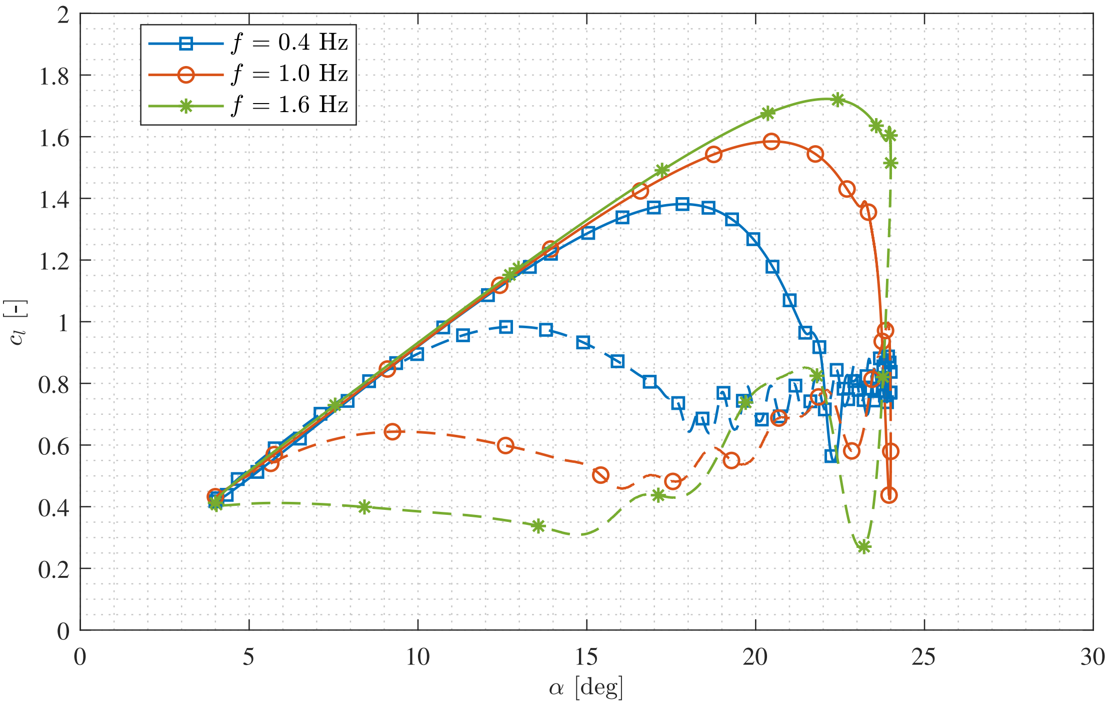

Fig. 3.19: Comparison of the lift coefficient c_l results for a motion of $\alpha_0 = 14$ deg and $\alpha_1 = 10$ deg at different frequencies: $f = 0.4$ Hz, $f = 1$ Hz and $f = 1.6$ Hz. Upstroke in solid line and downstroke in dashed line.

At small incidences, all three cases have a similar slope. However, discrepancies between the cases start when incidence increases beyond the static stall angle. The lowest frequency case soon reaches its maximum lift coefficient, $c_{lm}|^1 = 1.375$ and then decreases relatively smoothly until $\alpha_{ds}|^1 = 21.5$ deg. At this angle, a dynamic stall state is reached, characterised by a small lift overshoot and a sudden decrease of the lift force $\Delta c_l|^1 = 0.4$. A high-frequency vortex shedding is generated with lift oscillations until the incidence is low enough to let the flow reattach.

As the frequency is increased, the maximum c_l is also larger, with $c_{lm}|^2 = 1.575$ and $c_{lm}|^3 = 1.725$; and the dynamic stall is developed at higher incidences $\alpha_{ds}|^2 = 23.25$ deg and $\alpha_{ds}|^3 = 24$ deg. Besides, the strength of the lift drop also increases in the medium-frequency and high-frequency cases, $\Delta c_l|^2 = 0.975$ and $\Delta c_l|^3 = 1.4$, respectively. Furthermore, the vortex shedding frequency is lower, and the amplitude of the oscillations is higher. Lastly, it can be stated that the reattachment incidence is also lower for higher frequencies. All of this leads to increasing the hysteresis loop with the frequency.

As seen in Figure 3.20, the PDSV size grows with the frequency. Moreover, it is developed relatively far from the aerofoil in the low-frequency case, consequently producing less effect on the lift coefficient.

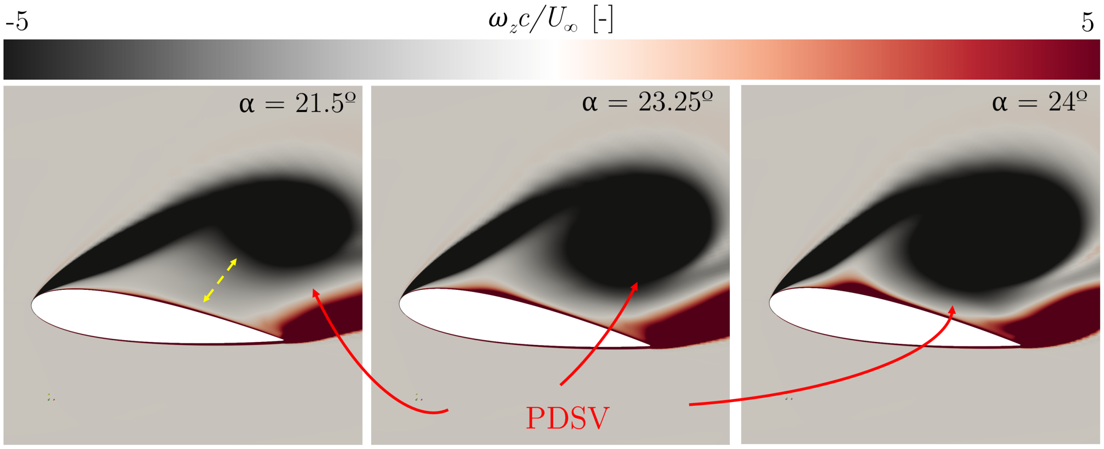

Fig. 3.20: Comparison of the dimensionless vorticity $\omega_z c/U_\infty$ around the aerofoil at the PDSV development instant for the small (1), medium (2) and high (3) frequency cases.

Amplitude

Secondly, the amplitude influence will be studied. Again, several cases are prepared: (1) very low ($\alpha_1 = 6$ deg), (2) low ($\alpha_1 = 8$ deg), (3) medium ($\alpha_1 = 10$ deg) and (4) high ($\alpha_1 = 14$ deg) amplitude motions are solved. A base mean angle $\alpha_0 = 14$ deg and reduced frequency $k = 0.063$ are chosen.

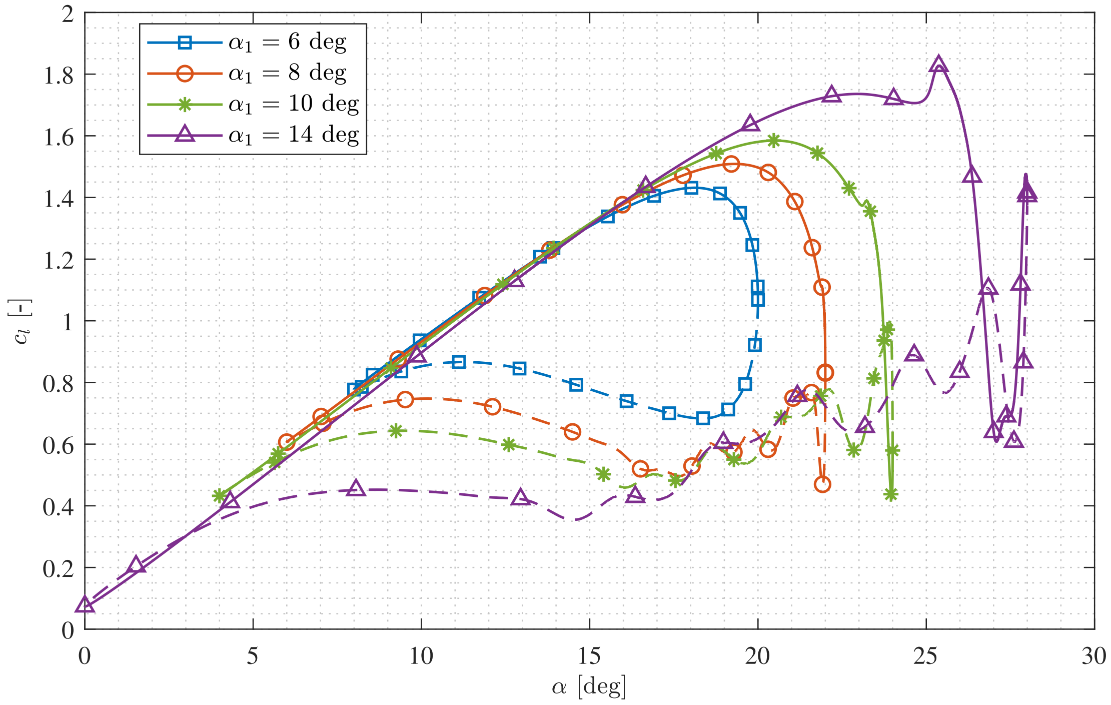

Fig. 3.21: Comparison of the lift coefficient c_l results for a motion of $\alpha_0 = 14$ deg and $k = 0.063$ at different amplitudes: $\alpha_1 = 6$ deg, $\alpha_1 = 8$ deg, $\alpha_1 = 10$ deg and $\alpha_1 = 14$ deg. Upstroke in solid line and downstroke in dashed line.

As it can be seen Figure 3.21, for the very low amplitude case, a light dynamic stall is produced (Figure 3.22). As it was stated in section 1.4, light dynamic stall develops when the maximum angle α_m is kept under a minimum threshold angle. In this case, it is larger than $\alpha_m|^1 = 20$ deg. Thus, no lift overshoot, sudden lift decay and vortex shedding appear during the motion. In this case, the maximum lift coefficient is $c_{lm}|^1 = 1.425$.

When the amplitude is increased by two degrees, a deep dynamic stall regime is developed, as a sudden lift decrease of $\Delta c_l|^2 = 0.6$ is produced at $\alpha_{ds}|^2 = 22$ deg. Besides, the maximum lift coefficient is larger, $c_{lm}|^2 = 1.5$. The same tendency is followed when the amplitude is increased further until the medium and high ones, with $c_{lm}|^3 = 1.575$ and $\Delta c_l|^3 = 0.975$ at $\alpha_{ds}|^3 = 23.25$ deg; and $c_{lm}|^4 = 1.825$ and $\Delta c_l|^4 = 1.225$ at $\alpha_{ds}|^4 = 25.5$ deg. Moreover, the vortex shedding during the downstroke motion is stronger when the amplitude is increased, and the hysteresis loop is also larger.

Lastly, in Figure 3.23 it can be seen a comparison between the results of 2D and 3D cases for the very small and high amplitudes. Due to their similarities, it can be stated that there is no significant difference between solving the case using a three-dimensional approach and a two-dimensional one in terms of accuracy. Thus, the 2D method is considered the best for studying this phenomenon, as the computational cost associated is much lower.

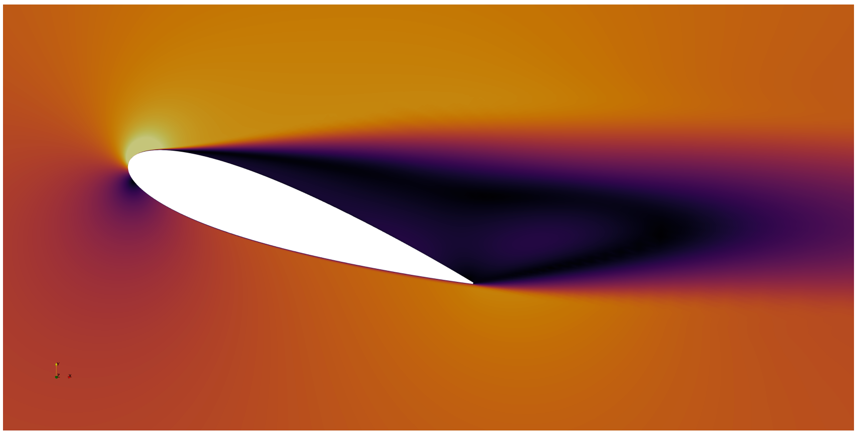

Fig. 3.22: Dimensionless velocity U/U_∞ field showing the light stall regime at $\alpha = 19$ deg (downstroke) for the low amplitude case ($\alpha_1 = 6$ deg).

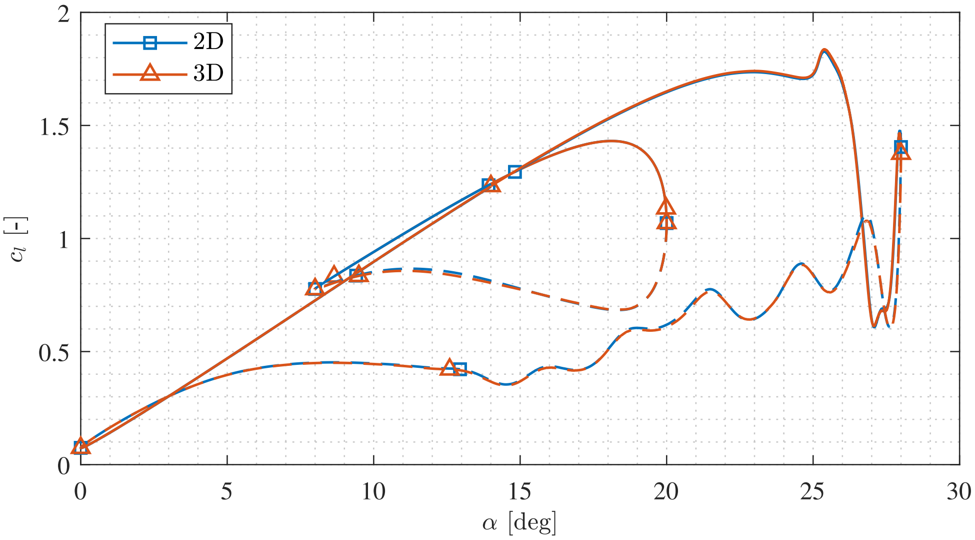

Fig. 3.23: Comparison of the lift coefficient c_l results for a motion of $\alpha_0 = 14$ deg and $k = 0.063$ at different amplitudes ($\alpha_1 = 6$ deg and $\alpha_1 = 14$ deg) using 2D and 3D simulations. Upstroke in solid line and downstroke in dashed line.

Turbulence intensity

Lastly, it was tried to perform a parametric study changing the inlet turbulence intensity, as it is one relevant factor in the dynamic stall behaviour. For this, a motion of mean angle $\alpha_0 = 14$ deg, amplitude $\alpha_0 = 14$ deg and reduced frequency $k = 0.063$ is considered. Results are shown in Figure 3.24.

The lift coefficient evolution obtained for the four cases suggests that the turbulence intensity has a minor influence on the dynamic stall behaviour. However, it was found that the reason for similar solutions for these cases is that the imposed TI at the inlet boundary condition decays along with the domain until it reaches the aerofoil. As it can be seen in Figure 3.25, for the higher TI case, it decreases from $TI = 7.5\%$ until $TI \approx 2\%$. Thus, it was not possible to study the actual turbulence intensity influence on the dynamic stall. Possible solutions to this could be changing the domain shape, placing the inlet closer to the aerofoil, or placing some vortex generators upstream of the aerofoil to induce turbulence in the flow.

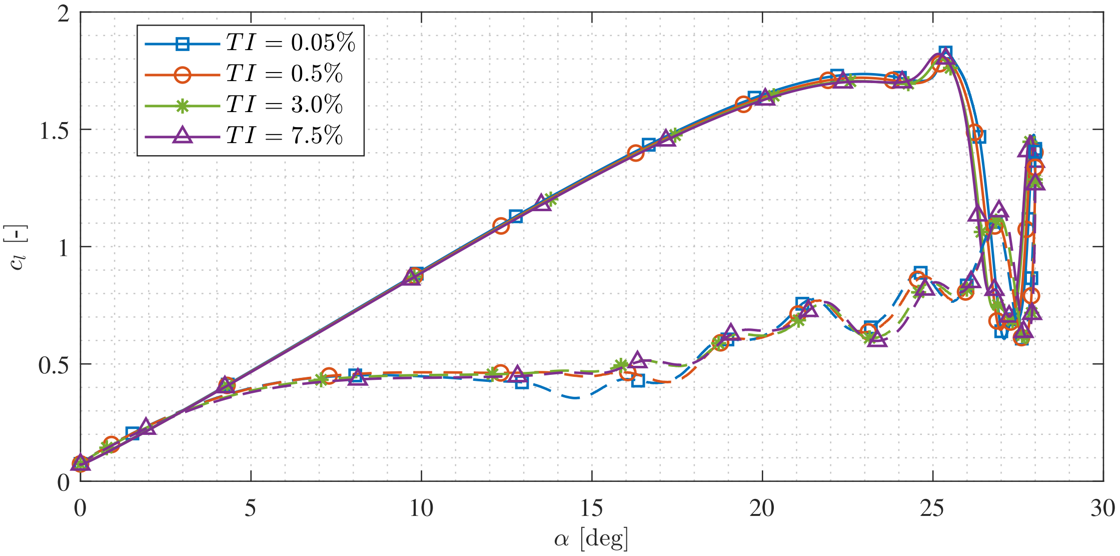

Fig. 3.24: Comparison of the lift coefficient c_l results for a motion of $\alpha_0 = 14$ deg, $\alpha_1 = 14$ deg and $k = 0.063$ with different inlet turbulence intensities: $TI = 0.05\%$, $TI = 0.5\%$, $TI = 3.0\%$ and $TI = 7.5\%$. Upstroke in solid line and downstroke in dashed line.

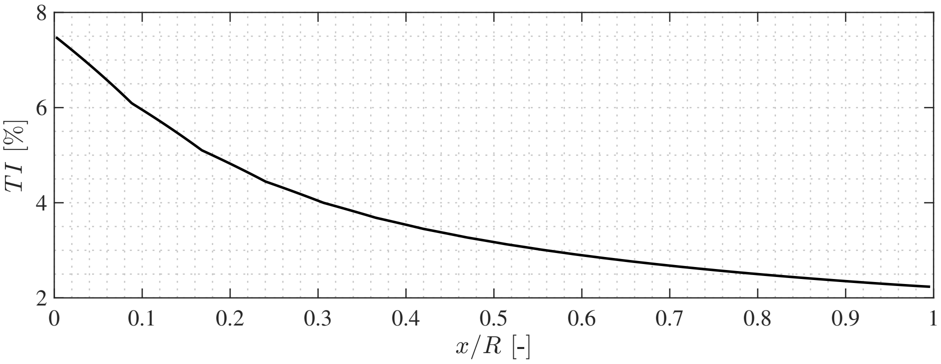

Fig. 3.25: Turbulence intensity evolution along with the x/R coordinate at $y/c = 0$ for the $TI = 7.5\%$ case.

Chapter 4

Conclusions and future developments

This chapter contains the most important conclusions that can be derived from the realisation of this project, reviewing whether the objectives have been reached or not. First of all, an extensive literature review has been carried out, identifying the essential characteristics of the dynamic stall. Thus, a description of the stall phases, a classification between light and deep stall regimes and the determination of the most influential parameters have been done.

Then, an optimal CFD setup has been developed, studying the main modelling alternatives and critically analysing each of them in terms of computational cost and accuracy. On the one hand, the DES approach results agree with the experimental data for the static cases until $\alpha \approx 15$ deg. It would be necessary to evaluate its precision at higher incidence for unsteady cases, but its computational cost is not affordable for this kind of project. On the other hand, URANS alternatives are accurate during the upstroke movement for the quasi-steady sweep, with deviation less than 10% at the maximum c_l prediction, but cannot reproduce the downstroke flow evolution. Moreover, the three-dimensional URANS cases successfully predict the abrupt stall behaviour, but the two-dimensional ones are not accurate in this region. However, results are identical with these two approaches in the dynamic stall cases.

Furthermore, several URANS low-Re turbulence models have been tested for the quasi-steady case. The Spalart-Allmaras turbulence model cannot predict the post-abrupt stall behaviour and is the less accurate. The Langtry-Menter k-ω SST has the advantage of correctly predicting the laminar separation bubble at this Reynolds number. However, the numerical instability and the higher computational cost make the base k-ω SST the best model for studying the dynamic stall in this project. Thus, the two-dimensional URANS approach with the k-ω SST model has been determined to be the best one as it represents a good accuracy while maintaining an affordable computational cost.

Moreover, the URANS k-ω SST simulations can predict the primary dynamic stall vortex, induced vortices and trailing edge vortex generation and detachment, with coherent flow evolution compared to literature.

Lastly, the influence of two crucial motion parameters has been studied. The increase in the frequency and amplitude leads to an increase in the maximum lift coefficient, a delayed dynamic stall onset, an enlargement of the stall strength, and a growth of the hysteresis loop size. On the other hand, the comparison between different turbulence intensities could not be made due to the turbulence intensity dissipation through the domain in the CFD simulations.

Future developments could be performed to follow and complete the analysis started in this project. Some of them are:

- To run the quasi-steady sweep at the same frequency as the experimental data ($f = 0.001$ Hz) to determine the actual accuracy of two-dimensional URANS simulations in this case.
- To elaborate DES simulations with the quasi-steady motion to analyse its accuracy with respect to 2D URANS cases.
- To develop a more robust setup around the Langtry-Menter turbulence model to simulate the quasi-steady motion at the experimental data turbulence intensity ($TI \approx 0.05\%$).
- To model the experimental wind tunnel to analyse the influence of the flow-wall interaction on the abrupt stall region.
- To validate the dynamic stall cases of the NACA0018 aerofoil with future experimental data.
- To solve the turbulence intensity decay problem by placing small-size obstacles upstream from the aerofoil.
- To perform other parametric studies such as the aerofoil geometry, kind of motion or Reynolds number to study its influence on the dynamic stall phenomenon.

Bibliography

[1] Johnson, Forrester T., Edward N. Tinoco, and N. Jong Yu: *Thirty years of development and application of CFD at Boeing Commercial Airplanes, Seattle.* Computers Fluids, 34(10):1115–1151, 2005, ISSN 0045-7930.

[2] Mulleners, Karen and M. Raffel: *Dynamic stall development.* Experiments in Fluids, 54, February 2013.

[3] Visbal, Miguel and Stuart I. Benton: *Exploration of High-Frequency Control of Dynamic Stall Using Large-Eddy Simulations.* AIAA Journal, 56(8):2974–2991, 2018.

[4] Singh, Chrisminder, David Peake, Anastasios Kokkalis, Vahik Khodagolian, F.N. Coton, and Ram Galbraith: *Control of Rotorcraft Retreating Blade Stall Using Air-Jet Vortex Generators.* Journal of Aircraft, 43, July 2006.

[5] Ma, Lu, Xiaodong Wang, Jian Zhu, and Shun Kang: *Dynamic Stall of a Vertical-Axis Wind Turbine and Its Control Using Plasma Actuation.* Energies, 12(19), 2019, ISSN 1996-1073.

[6] Ouro, Pablo, Thorsten Stoesser, and Luis Ramírez: *Effect of Blade Cambering on Dynamic Stall in View of Designing Vertical Axis Turbines.* Journal of Fluids Engineering, Transactions of the ASME, 140(6):1–12, 2018, ISSN 1528901X.

[7] Mulleners, Karen and Markus Raffel: *The onset of dynamic stall revisited.* Experiments in Fluids, 52(3):779–793, 2012, ISSN 07234864.

[8] Jain, Siddhant and Ujjwal K. Saha: *On the influence of blade thickness-to-chord ratio on dynamic stall phenomenon in H-type Darrieus wind rotors.* Energy Conversion and Management, 218:113024, 2020, ISSN 0196-8904.

[9] Xiao, Heng and Paola Cinnella: *Quantification of model uncertainty in RANS simulations: A review.* Progress in Aerospace Sciences, 108(April):1–31, 2019, ISSN 03760421.

[10] Akan, Cigdem: *Surface Mass Transfer in Large Eddy Simulation (LES) of Langmuir Turbulence.* January 2012.

[11] Strangfeld, C., C. L. Rumsey, H. Müller-Vahl, D. Greenblatt, C. N. Nayeri, and C. O. Paschereit: *Unsteady thick airfoil aerodynamics: Experiments, computation, and theory.* 45th AIAA Fluid Dynamics Conference, pages 1–19, 2015.

[12] Timmer, W. A.: *Two-dimensional low-Reynolds number wind tunnel results for airfoil NACA 0018.* Wind Engineering, 32(6):525–537, 2008, ISSN 0309524X.

[13] Mccroskey, W. J.: *The phenomenon of dynamic stall.* Technical report, 1981.

[14] Buchner, A J., M.W. Lohry, L. Martinelli, J. Soria, and A.J. Smits: *Dynamic stall in vertical axis wind turbines: Comparing experiments and computations.* Journal of Wind Engineering and Industrial Aerodynamics, 146:163–171, 2015, ISSN 0167-6105.

[15] McCroskey, W.J., L.W. Carr, and K.W. McAlister: *Dynamic Stall Experiments on Oscillating Airfoils.* AIAA Journal, 14(1):57–63, 1976.

[16] McCroskey, Mcalister, Carr, and Pucci: *An experimental study of dynamic stall on advanced airfoil sections. Volume 1: Summary of the experiment.* Technical report, 1982.

[17] Wernert, Philippe, W. Geißler, Juergen Kompenhans, and M. Raffel: *Experimental and numerical investigations of dynamic stall on a pitching airfoil.* Aiaa Journal - AIAA J, 34:982–989, May 1996.

[18] Zhou, Teng, Yuhao Sun, Ryu Fattah, Xin Zhang, and Xun Huang: *An experimental study of trailing edge noise from a pitching airfoil.* The Journal of the Acoustical Society of America, 145(4):2009–2021, 2019.

[19] Sheldahl, R E and P C Klimas: *Aerodynamic characteristics of seven symmetrical airfoil sections through 180-degree angle of attack for use in aerodynamic analysis of vertical axis wind turbines.* March 1981.

[20] Jacobs, Eastman N. and Albert Sherman: *Airfoil section characteristics as affected by variations of the Reynolds number.* 1939.

[21] Wickens, R.H.: *Wind tunnel investigation of dynamic stall of a NACA 0018 Airfoil oscillating in Pitch*, 1985, ISBN 9781624103629.

[22] Raghunathan, S. and O. O. Ombaka: *A thick symmetrical aerofoil oscillating about zero incidence angle.* International Journal of Heat and Fluid Flow, 7(2):155–159, 1986, ISSN 0142727X.

[23] Swalwell, K, John Sheridan, and W Melbourne: *The effect of turbulence intensity on stall of the NACA 0021 aerofoil.* 14th Australasian Fluid Mechanics Conference, pages 941–944, January 2001.

[24] Geissler, W., G. Dietz, and H. Mai: *Dynamic stall on a supercritical airfoil.* Aerospace Science and Technology, 9(5):390–399, 2005, ISSN 12709638.

[25] Wang, Shengyi, Derek B. Ingham, Lin Ma, Mohamed Pourkashanian, and Zhi Tao: *Numerical investigations on dynamic stall of low Reynolds number flow around oscillating airfoils.* Computers and Fluids, 39(9):1529–1541, 2010, ISSN 00457930.

[26] Honarmand, Mojtaba, Mohammad Hassan Djavareshkian, Behzad Forouzi Feshalami, and Esmaeil Esmaeilifar: *Numerical simulation of a pitching airfoil under dynamic stall of low reynolds number flow.* Journal of Aerospace Technology and Management, 11(2010):1–14, 2019, ISSN 21759146.

[27] Bangga, Galih, Go Hutomo, Raditya Wiranegara, and Herman Sasongko: *Numerical study on a single bladed vertical axis wind turbine under dynamic stall.* Journal of Mechanical Science and Technology, 31(1):261–267, 2017, ISSN 1738494X.

[28] Bangga, Galih: *Numerical studies on dynamic stall characteristics of a wind turbine airfoil.* Journal of Mechanical Science and Technology, 33(3):1257–1262, 2019, ISSN 1738494X.

[29] Gleize, Vincent, Michel Costes, Arnaud Le Pape, and F. Richez: *Numerical Simulation of a Pitching Airfoil Under Dynamic Stall Conditions Including Laminar/Turbulent Transition.*

[30] Wang, Shengyi, Derek B. Ingham, Lin Ma, Mohamed Pourkashanian, and Zhi Tao: *Turbulence modeling of deep dynamic stall at relatively low Reynolds number.* Journal of Fluids and Structures, 33:191–209, 2012, ISSN 0889-9746.

[31] Chitsomboon, Tawit and Chalothorn Thamthae: *Adjustment of k-w SST Turbulence Model for an Improved Prediction of Stalls on Wind Turbine Blades.* Proceedings of the World Renewable Energy Congress – Sweden, 8–13 May, 2011, Linköping, Sweden, 57(November 2011):4114–4120, 2011.

[32] Bangga, G. and H. Sasongko: *Dynamic stall prediction of a pitching airfoil using an adjusted two-equation URANS turbulence model.* Journal of Applied Fluid Mechanics, 10(1):1–10, 2017, ISSN 17353645.

[33] Zhang, Kailing, Jinping Li, Fanzhi Zeng, Qiang Wang, and Chao Yan: *Uncertainty Analysis of Parameters in SST Turbulence Model for Shock Wave-Boundary Layer Interaction.* Aerospace, 9(2):1–20, 2022, ISSN 22264310.

[34] Zhong, Wei, Hongwei Tang, Tongguang Wang, and Chengyong Zhu: *Accurate RANS simulation of wind turbine stall by turbulence coefficient calibration.* Applied Sciences (Switzerland), 8(9), 2018, ISSN 20763417.

[35] Matyushenko, A. A. and A. V. Garbaruk: *Adjustment of the k-ω SST turbulence model for prediction of airfoil characteristics near stall.* Journal of Physics: Conference Series, 769(1), 2016, ISSN 17426596.

[36] Khalifa, Nabil M., Amir S. Rezaei, and Haitham E. Taha: *Comparing the Performance of Different Turbulence Models in Predicting Dynamic Stall.*

[37] Ferreira, Carlos, Hester Bijl, Gerard van Bussel, and Gijs Kuik: *Simulating Dynamic Stall in a 2D VAWT: Modeling strategy, verification and validation with Particle Image Velocimetry data.* Journal of Physics: Conference Series, 75 (1), 75, June 2007.

[38] Abdulqadir, Sherwan A., Hector Iacovides, and Adel Nasser: *The physical modelling and aerodynamics of turbulent flows around horizontal axis wind turbines.* Energy, 119:767–799, 2017, ISSN 03605442.

[39] Hand, Brian, Ger Kelly, and Andrew Cashman: *Numerical simulation of a vertical axis wind turbine airfoil experiencing dynamic stall at high Reynolds numbers.* Computers Fluids, 149:12–30, 2017, ISSN 0045-7930.

[40] *Pointwise, Inc.* `http://https://www.pointwise.com/`. Accessed: 2022-05-10.

[41] *NASA: Examining Spatial (Grid) Convergence.* `https://www.grc.nasa.gov/www/wind/valid/tutorial/spatconv.html`. Accessed: 2022-05-11.

[42] Spalart, Philippe and Steven Allmaras: *A One-Equation Turbulence Model for Aerodynamic Flows.* AIAA, 439, January 1992.

[43] *NASA Turbulence Modeling Resource. Spalart-Allmaras.* `https://turbmodels.larc.nasa.gov/spalart.html`. Accessed: 2022-05-13.

[44] Menter, F. R.: *Two-equation eddy-viscosity turbulence models for engineering applications.* August 1994.

[45] *NASA Turbulence Modeling Resource. k-ω SST.* `https://turbmodels.larc.nasa.gov/sst.html`. Accessed: 2022-05-13.

[46] Langtry, Robin B. and Florian R. Menter: *Correlation-Based Transition Modeling for Unstructured Parallelized Computational Fluid Dynamics Codes.* AIAA Journal, 47(12):2894–2906, 2009.

[47] *NASA Turbulence Modeling Resource. Langtry-Menter k-ω SST.* `https://turbmodels.larc.nasa.gov/langtrymenter_4eqn.html`. Accessed: 2022-05-13.